The Astrophysical Journal, 1010:237 (20pp), 2026 October 20 https://doi.org/10.3847/1538-4357/ae8d09
© 2026. The Author(s). Published by the American Astronomical Society.
OPEN ACCESS

VENUS: A Strongly Lensed Clumpy Galaxy at $z \sim 11$–12 Behind the Galaxy Cluster MACS J0257.1-2325

Minami Nakane[1,2], Vasily Kokorev[3,4], Seiji Fujimoto[5,6], Masami Ouchi[1,7,8,9], Derek J. McLeod[10], Miriam Golubchik[11], Masamune Oguri[12,13], Adi Zitrin[11], Cecilia Bondestam[10], Callum T. Donnan[14], Gabriel Brammer[15,16], Steven L. Finkelstein[3,4], Chris Willott[17], Gregor Rihtaršič[18], Guillaume Desprez[19], Angela Adamo[20], Eros Vanzella[21], Maruša Bradač[22,23], Matteo Messa[21], Hiroto Yanagisawa[1,2], Fengwu Sun[24], Henry C. Ferguson[25], Ray A. Lucas[25], Dan Coe[26,27,28], Johan Richard[29], Abdurro'uf[30], Hollis B. Akins[3], Joseph F. V. Allingham[31], Ricardo O. Amorín[32], Yoshihisa Asada[6], Hakim Atek[33], Franz E. Bauer[34], Rachel Bezanson[35], Larry D. Bradley[25], John Chisholm[3,4], Christopher J. Conselice[36], Pratika Dayal[37,38,39], Miroslava Dessauges-Zavadsky[40], Jose M. Diego[41], Andreas L. Faisst[42], Gavin Farley[43], Qinyue Fei[5], Brenda L. Frye[44], Yoshinobu Fudamoto[12], Lukas J. Furtak[4,45], Yuichi Harikane[1], Tiger Yu-Yang Hsiao[3,4], Yolanda Jiménez-Teja[32,46], Jeyhan S. Kartaltepe[47], Tomokazu Kiyota[7,48], Anton M. Koekemoer[25], Claudia del P. Lagos[49,50], Georgios E. Magdis[15,51], Ashish Kumar Meena[52], Lamiya Mowla[53], Gaël Noirot[25], Pascal A. Oesch[15,40], Yoshiaki Ono[1], Rafael Ortiz, III[54], Richard Pan[55], Casey Papovich[56,57], Justin D. R. Pierel[25], Massimo Ricotti[58], Luke Robbins[59], Daniel Schaerer[40,60], Raffaella Schneider[61], Tommaso Treu[62], Francesco Valentino[15,63], Rogier A. Windhorst[54], Volker Bromm[3,4,64], Eiichi Egami[65], Mauro González-Otero[32], Kotaro Kohno[66,67], Ivo Labbe[68], Jorryt Matthee[69], Marcie Mun[33], Rohan P. Naidu[70], and Roberta Tripodi[71,72,73]

[1] Institute for Cosmic Ray Research, The University of Tokyo, 5-1-5 Kashiwanoha, Kashiwa, Chiba 277-8582, Japan; nakanem@icrr.u-tokyo.ac.jp
[2] Department of Physics, Graduate School of Science, The University of Tokyo, 7-3-1 Hongo, Bunkyo, Tokyo 113-0033, Japan
[3] Department of Astronomy, The University of Texas at Austin, 2515 Speedway, Stop C1400, Austin, TX 78712, USA
[4] Cosmic Frontier Center, The University of Texas at Austin, Austin, TX 78712, USA
[5] David A. Dunlap Department of Astronomy and Astrophysics, University of Toronto, 50 St. George Street, Toronto, Ontario, M5S 3H4, Canada
[6] Dunlap Institute for Astronomy and Astrophysics, 50 St. George Street, Toronto, Ontario, M5S 3H4, Canada
[7] National Astronomical Observatory of Japan, 2-21-1 Osawa, Mitaka, Tokyo 181-8588, Japan
[8] Department of Astronomical Science, SOKENDAI (The Graduate University for Advanced Studies), 2-21-1 Osawa, Mitaka, Tokyo 181-8588, Japan
[9] Kavli Institute for the Physics and Mathematics of the Universe (WPI), The University of Tokyo, 5-1-5 Kashiwanoha, Kashiwa, Chiba 277-8583, Japan
[10] Institute for Astronomy, University of Edinburgh, Royal Observatory, Edinburgh EH9 3HJ, UK
[11] Department of Physics, Ben-Gurion University of the Negev, PO Box 653, Beer-Sheva 8410501, Israel
[12] Center for Frontier Science, Chiba University, 1-33 Yayoi-cho, Inage-ku, Chiba 263-8522, Japan
[13] Department of Physics, Graduate School of Science, Chiba University, 1-33 Yayoi-Cho, Inage-Ku, Chiba 263-8522, Japan
[14] NSF's National Optical-Infrared Astronomy Research Laboratory, 950 N. Cherry Avenue, Tucson, AZ 85719, USA
[15] Cosmic Dawn Center (DAWN), Denmark
[16] Niels Bohr Institute, University of Copenhagen, Jagtvej 128, 2200 Copenhagen N, Denmark
[17] NRC Herzberg, 5071 West Saanich Road, Victoria, BC V9E 2E7, Canada
[18] University of Ljubljana, Faculty of Mathematics and Physics, Jadranska ulica 19, SI-1000 Ljubljana, Slovenia
[19] Kapteyn Astronomical Institute, University of Groningen, PO Box 800, 9700AV Groningen, The Netherlands
[20] Department of Astronomy, The Oskar Klein Centre, Stockholm University, AlbaNova, SE-10691 Stockholm, Sweden
[21] INAF—OAS, Osservatorio di Astrofisica e Scienza dello Spazio di Bologna, via Gobetti 93/3, I-40129 Bologna, Italy
[22] University of Ljubljana, Department of Mathematics and Physics, Jadranska ulica 19, SI-1000 Ljubljana, Slovenia
[23] Department of Physics and Astronomy, University of California Davis, 1 Shields Avenue, Davis, CA 95616, USA
[24] Center for Astrophysics|Harvard & Smithsonian, 60 Garden Street, Cambridge, MA 02138, USA
[25] Space Telescope Science Institute, 3700 San Martin Drive, Baltimore, MD 21218, USA
[26] Space Telescope Science Institute (STScI), 3700 San Martin Drive, Baltimore, MD 21218, USA
[27] Center for Astrophysical Sciences, Department of Physics and Astronomy, The Johns Hopkins University, 3400 N Charles Street, Baltimore, MD 21218, USA
[28] Association of Universities for Research in Astronomy (AURA), Inc. for the European Space Agency (ESA), USA
[29] Univ Lyon, Univ. Lyon 1, Ens de Lyon, CNRS, Centre de Recherche Astrophysique de Lyon UMR5574, F-69230, Saint-Genis-Laval, France
[30] Department of Astronomy, Indiana University, 727 East Third Street, Bloomington, IN 47405, USA
[31] Department of Physics, Ben-Gurion University of the Negev, PO Box 653, Be'er-Sheva 84105, Israel
[32] Instituto de Astrofísica de Andalucía–CSIC, Glorieta de la Astronomía s/n, E–18008 Granada, Spain
[33] Institut d'Astrophysique de Paris, CNRS, Sorbonne Université, 98bis Boulevard Arago, 75014, Paris, France
[34] Instituto de Alta Investigación, Universidad de Tarapacá, Casilla 7D, Arica, 1010000, Chile
[35] Department of Physics and Astronomy and PITT PACC, University of Pittsburgh, Pittsburgh, PA 15260, USA
[36] Jodrell Bank Centre for Astrophysics, University of Manchester, Oxford Road, Manchester M13 9PL, UK
[37] Canadian Institute for Theoretical Astrophysics, 60 St George St, University of Toronto, Toronto, ON M5S 3H8, Canada
[38] David A. Dunlap Department of Astronomy and Astrophysics, University of Toronto, 50 St George Street, Toronto ON M5S 3H4, Canada
[39] Department of Physics, University of Toronto, 60 St. George Street, Toronto, ON M5S 3H8, Canada
[40] Department of Astronomy, University of Geneva, Chemin Pegasi 51, 1290 Versoix, Switzerland
[41] Instituto de Física de Cantabria (CSIC-UC), Avenida Lastros s/n. 39005 Santander, Spain
[42] IPAC, California Institute of Technology, 1200 E. California Boulevard Pasadena, CA 91125, USA
[43] David A. Dunlap Department of Astronomy & Astrophysics, University of Toronto, 50 St. George Street, Toronto, ON M5S 3H4, Canada
[44] Department of Astronomy/Steward Observatory, University of Arizona, 933 N. Cherry Avenue, Tucson, AZ 85721, USA
[45] Department of Astronomy, The University of Texas at Austin, Austin, TX 78712, USA
[46] Observatório Nacional, Rua General José Cristino, 77 - Bairro Imperial de São Cristóvão, Rio de Janeiro, 20921-400, Brazil
[47] Laboratory for Multiwavelength Astrophysics, School of Physics and Astronomy, Rochester Institute of Technology, 84 Lomb Memorial Drive, Rochester, NY 14623, USA
[48] Department of Astronomical Science, The Graduate University for Advanced Studies, SOKENDAI, 2-21-1 Osawa, Mitaka, Tokyo 181-8588, Japan
[49] International Centre for Radio Astronomy Research, The University of Western Australia, 35 Stirling Highway, Crawley, WA6009, Australia

[50] ARCCentre of Excellence for All Sky Astrophysics in 3 Dimensions (ASTRO 3D), Canberra, ACT 2611, Australia
[51] DTU-Space, Technical University of Denmark, Elektrovej 327, 2800, Kgs. Lyngby, Denmark
[52] Department of Physics, Indian Institute of Science, Bengaluru 560012, India
[53] Department of Physics and Astronomy, Wellesley College, Wellesley, MA 02481, USA
[54] School of Earth and Space Exploration, Arizona State University, Tempe, AZ 85287-6004, USA
[55] Department of Physics & Astronomy, Tufts University, Medford, MA 02155, USA
[56] Department of Physics and Astronomy, Texas A&M University, College Station, TX 77843-4242, USA
[57] George P. and Cynthia Woods Mitchell Institute for Fundamental Physics and Astronomy, Texas A&M University, College Station, TX 77843-4242, USA
[58] Department of Astronomy, University of Maryland, College Park 20742, USA
[59] Department of Physics and Astronomy, Tufts University, Medford, MA 02155, USA
[60] CNRS, IRAP, 14 Avenue Edouard Belin, 31400 Toulouse, France
[61] Department of Physics, Sapienza University of Rome, Pzz.le Aldo Moro 5, 00185 Rome, Italy
[62] Department of Physics and Astronomy, University of California, Los Angeles, CA 90095, USA
[63] DTU Space, Technical University of Denmark, Elektrovej 327, DK-2800 Kgs. Lyngby, Denmark
[64] Weinberg Institute for Theoretical Physics, Texas Center for Cosmology and Astroparticle Physics, University of Texas at Austin, Austin, TX 78712, USA
[65] Steward Observatory, University of Arizona, 933 N. Cherry Avenue, Tucson AZ85721, USA
[66] Institute of Astronomy, Graduate School of Science, The University of Tokyo, 2-21-1 Osawa, Mitaka, Tokyo, 181-0015, Japan
[67] Research Center for the Early Universe, Graduate School of Science, The University of Tokyo, 7-3-1 Hongo, Bunkyo-ku, Tokyo 113-0033, Japan
[68] Centre for Astrophysics and Supercomputing, Swinburne University of Technology, Melbourne, VIC 3122, Australia
[69] Institute of Science and Technology Austria (ISTA), Am Campus 1, 3400 Klosterneuburg, Austria
[70] MIT Kavli Institute for Astrophysics and Space Research, 70 Vassar Street, Cambridge, MA 02139, USA
[71] INAF—Osservatorio Astronomico di Roma, Via Frascati 33, I-00078 Monte Porzio Catone, Italy
[72] University of Ljubljana FMF, Jadranska 19, 1000 Ljubljana, Slovenia
[73] IFPU, Institute for Fundamental Physics of the Universe, Via Beirut 2, 34014 Trieste, Italy
Received 2025 November 18; revised 2026 July 16; accepted 2026 July 16; published 2026 October 19

Abstract

We present the discovery of a strongly lensed galaxy at $z \sim 11$–12, dubbed the "Misty Moons," identified in the JWST Treasury Survey, Vast Exploration for Nascent, Unexplored Sources. The Misty Moons is gravitationally lensed by the galaxy cluster MACS J0257.1-2325 at $z = 0.505$, and has five multiple images suggested by two independent lens models. Two of the five images, ID1 and ID2 ($\mu \sim 20$–30), are very bright (F200W$\sim$26 AB mag) and exhibit blue SEDs with prominent Lyα breaks. In the source plane, the Misty Moons is a sub-L^* galaxy ($M_{\rm UV} \sim -18.0$ mag) resolved into multiple stellar clumps, each of which has an effective radius of $r_{\rm eff} \sim 10$–70 pc and a stellar mass of $\sim 10^7\,M_\odot$. These clumps dominate the stellar mass budget of the Misty Moons ($\gtrsim$80%), similar to other high-z clumps, which suggests a highly clustered mode of star formation in the early Universe, unlike seen in local dwarf galaxies. We convolve the source-plane image with the JWST/NIRCam point-spread function to produce a mock NIRCam image of the Misty Moons without lensing magnification and find that the intrinsic galaxy has a radial surface-brightness profile comparable to those of $z \gtrsim 10$ faint galaxies, such as JADES-GS-z13-0 and JADES-GS-z14-1, indicating that the Misty Moons represents a typical $z \gtrsim 10$ faint galaxy. The Misty Moons, a lensed galaxy with resolved internal structures, provides an ideal laboratory for exploring the early stages of galaxy formation at $z \gtrsim 10$.

Unified Astronomy Thesaurus concepts: Early universe (435); Galaxy clusters (584); Galaxy evolution (594); Galaxy formation (595); High-redshift galaxies (734); Star formation (1569); Strong gravitational lensing (1643)

1. Introduction

JWST observations have been unveiling the nature of early galaxies up to $z > 10$ (e.g., P. Arrabal Haro et al. 2023; E. Curtis-Lake et al. 2023; S. Carniani et al. 2024; R. P. Naidu et al. 2026). Some of the intrinsically bright galaxies at $z \gtrsim 6$, such as GHZ2 ($z_{\rm spec} = 12.34$; M. Castellano et al. 2024; J. A. Zavala et al. 2024) and GN-z11 ($z_{\rm spec} = 10.60$; A. J. Bunker et al. 2023; R. Maiolino et al. 2024), show compact morphologies with half-light radii of $r_{\rm eff} \lesssim 100$ pc and nitrogen-rich abundance ratios, suggesting a possible connection with globular clusters (GCs; e.g., Y. Isobe et al. 2023b, 2025; P. Senchyna et al. 2024; M. W. Topping et al. 2024, 2025; Y. Harikane et al. 2025; X. Ji et al. 2026). However, the stellar masses of these galaxies are more than 1 order of magnitude larger than typical local GCs, which suggests possibilities of superposition of several individual clusters and significant mass loss due to dynamical evolution (e.g., J. J. Webb & N. W. C. Leigh 2015; J. A. Zavala et al. 2024). In addition, these galaxies are not resolved into their components, which complicates a direct comparison. Gravitational lensing bridges this gap by boosting both signal-to-noise (S/N) ratio and spatial resolution. High magnification by gravitational lensing has enabled identifications of 1–10 pc scale star clusters or stellar clumps with stellar masses of $M_* \sim 10^4$–$10^7 M_\odot$ at $z \gtrsim 6$ (e.g., E. Vanzella et al. 2023; A. Adamo et al. 2024; L. D. Bradley et al. 2025; L. Mowla et al. 2024; Abdurro'uf et al. 2025; M. Bradač et al. 2025; S. Fujimoto et al. 2025; M. Messa et al. 2025, 2026). Overall, they share comparable properties of young stellar age, low metallicity, and low dust extinction. They also exhibit high stellar mass surface densities (Σ_*), some of which have about 3 orders of magnitude higher ($\Sigma_* > 10^5\,M_\odot\,{\rm pc}^{-2}$) than typical young star clusters in the local Universe (G. Brown & O. Y. Gnedin 2021).

Star cluster formation in the local Universe is quantitatively evaluated by the cluster formation efficiency (CFE), which is a fraction of total stellar mass of star clusters to that of their host

Original content from this work may be used under the terms of the Creative Commons Attribution 4.0 licence. Any further distribution of this work must maintain attribution to the author(s) and the title of the work, journal citation and DOI.

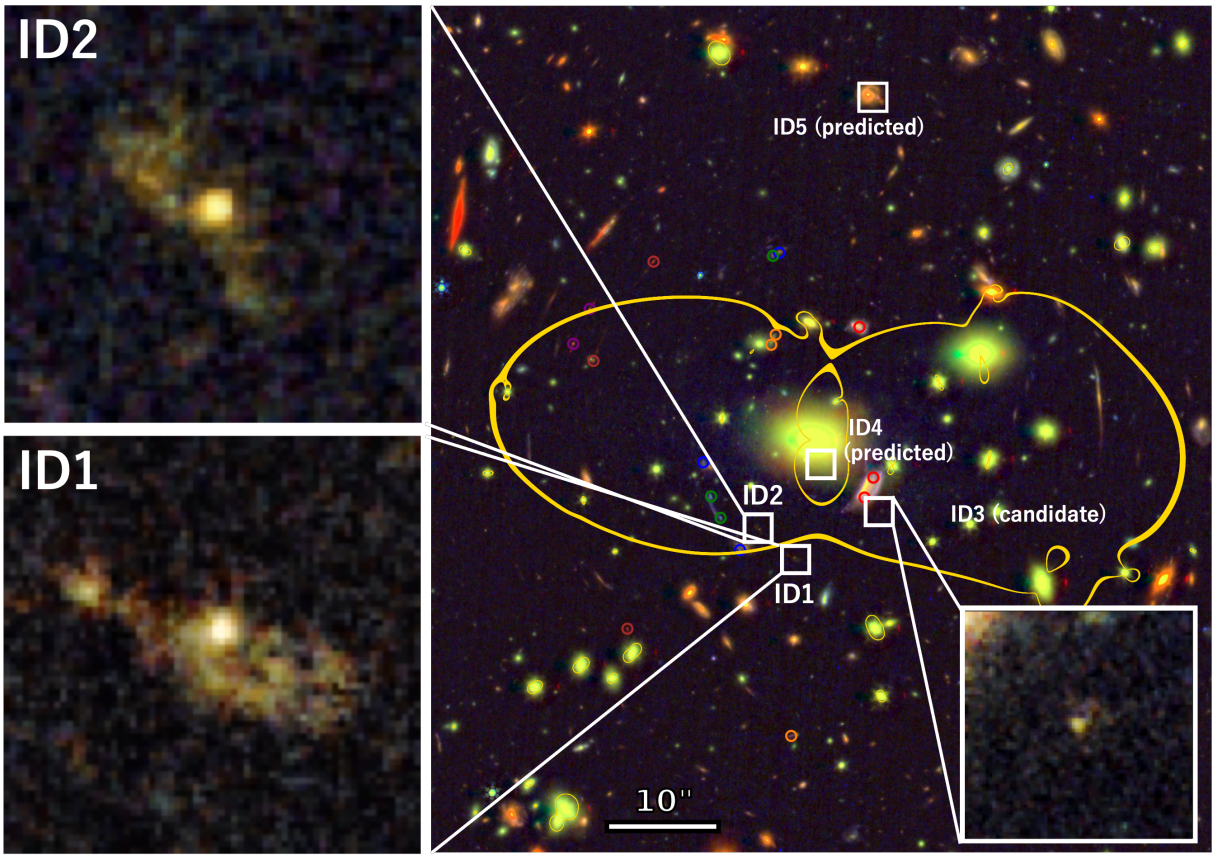


Figure 1. NIRCam RGB color image (R: F356W+F410M+F444W, G: F150W+F200W+F277W, B: F435W+F814W+F150W) of the MACS J0257.1-2325 cluster field. The yellow curve indicates the critical curve at $z = 11$–12. The white squares show the positions of ID1–ID5 of the Misty Moons predicted by our independent lens models while the colored circles denote the $z \sim 1$–8 multiple image systems used to constrain the lens models (see Section 3). $2'' \times 2''$ cutout images show the zoom in on ID1, ID2, and a candidate for ID3.

galaxy, formed in a given time interval (e.g., Q. E. Goddard et al. 2010; A. Adamo et al. 2011, 2020; J. M. D. Kruijssen 2012; M. Messa et al. 2018; D. O. Cook et al. 2023). These studies have suggested a positive correlation between the CFE and star formation rate (SFR) surface density ($\Sigma_{\rm SFR}$). An increasing trend of $\Sigma_{\rm SFR}$ with redshift for high-z star-forming galaxies (e.g., T. Morishita et al. 2024) indicates that the CFE in the early Universe could be high. A recent study of E. Vanzella et al. (2026) has investigated the CFE of the Cosmic Gems galaxy at $z_{\rm spec} = 9.63$, which contains 1 pc scale gravitationally bound star clusters (A. Adamo et al. 2024; L. D. Bradley et al. 2025; M. Messa et al. 2026). They conclude that the individual star clusters within the Cosmic Gems galaxy require a large CFE ($\Gamma = 50\%$–100%), together with a top-heavy star cluster mass function or a slope $\beta > -2$ with a higher minimum cluster mass limit, in order to reproduce the observed massive clusters. Currently, the detections of high-z galaxies, which are resolved into star cluster scales, remain rare, especially beyond $z \sim 10$, due to the relatively small volume probed at sufficiently high magnification required to observe such intrinsically faint objects. This motivates a search for highly magnified $z > 10$ galaxies across as many strong-lensing cluster fields as possible, to explore in detail the star cluster and clump formation in the early Universe.

In this work, we present the discovery of a strongly lensed and highly magnified clumpy galaxy at $z_{\rm phot} \sim 11$–12, dubbed the "Misty Moons" (Figure 1), identified in the Vast Exploration for Nascent, Unexplored Sources (VENUS) JWST/NIRCam images and the Reionization Lensing Cluster Survey (RELICS) HST images of the lensing galaxy cluster MACS J0257.1-2325 at $z = 0.505$. This paper is organized as follows. In Section 2, we describe our observations and photometric measurements. Section 3 details our lens models based on the latest NIRCam observations. In Section 4, we explain the analysis procedures including clump modeling and spectral energy distribution (SED) fitting. In Section 5, we present our results, and discuss the physical properties and clump formation of the Misty Moons. Section 6 summarizes our findings. Throughout this paper, we assume a standard ΛCDM cosmology with $\Omega_\Lambda = 0.7$, $\Omega_m = 0.3$, and $H_0 = 70\,{\rm km\,s^{-1}\,Mpc^{-1}}$. All magnitudes are in the AB system (J. B. Oke & J. E. Gunn 1983).

2. Observation and Photometry

2.1. JWST and HST Observations

The galaxy cluster MACS J0257.1-2325 (hereafter MACS0257-2325), located at $z = 0.505$, was observed with JWST/NIRCam as part of the treasury lensing cluster survey VENUS (Cycle 4 GO-6882, PIs: S. Fujimoto & D. Coe; S. Fujimoto et al. 2026, in preparation) on 18–19 August 2025. The NIRCam observations utilize 10 bands consisting of F090W, F115W, F150W, F200W, F210M, F277W, F300M, F356W, F410M, and F444W with exposure times of 0.35–0.57 hr to homogeneously achieve a source detection limit of $\sim$28 mag across all the NIRCam filters (5σ, point source). A dedicated paper describing the VENUS data reduction

procedure is forthcoming. Here, we only briefly describe our methodology. We start with JWST level-2 products from the Mikulski Archive for Space Telescopes (MAST) and reduce them with the `grizli` pipeline (G. Brammer 2023a, 2023b), similarly to the widely available public DAWN JWST Archive (DJA) products.[74] The photometric calibration was performed with the Calibration Reference Data System (CRDS) context `jwst_1456.pmap`. The `grizli` procedure implements crucial improvements over the standard STScI pipeline, including corrections for cosmic rays, stray light, and detector artifacts (L. D. Bradley et al. 2023; J. Rigby et al. 2023). Further, we implement additional background, $1/f$ noise and diffraction spike subtraction procedures, both at the amplifier level, for each filter, and then the final drizzled mosaic (e.g., see R. Endsley et al. 2024; V. Kokorev et al. 2025a). JWST NIRCam images are drizzled to a $0\farcs03$/pix grid. We also incorporate HST imaging of MACS J0257.1-2325 (D. Coe et al. 2019) obtained with ACS/WFC F435W, F555W, and F814W. The HST images are based on Gaia-aligned mosaics from the CHArGE archive (V. Kokorev et al. 2022), which are then drizzled on the same footprint and pixel scale as the JWST data.

From these imaging data, we searched for sources with high photometric redshifts and high lensing magnifications. We identified two multiple images of a $z \sim 11$–12 galaxy, which exhibit clear F150W dropouts with nondetections in all bands at shorter wavelengths and similar SED colors (Figure 2). Based on the independent lens models (see Section 3), five multiple images (ID1–ID5) are predicted for this galaxy, two of which, ID1 and ID2, are bright (F200W $\sim$ 26 mag) and exhibit complex morphologies owing to their high magnification ($\mu \sim 20$–30), as shown in Figure 1. On the other hand, the intrinsic UV magnitudes derived from the F200W fluxes are as low as $M_{\rm UV} \sim -18$ mag (see Figure 3 and Table 1). We also find a candidate for ID3, characterized by nondetections at short wavelengths (<1.5 μm) and blue SED just like ID1 and ID2. In the following sections, we mainly focus on the highly magnified multiple images of ID1 and ID2.

2.2. Photometry

We produce a detection image by taking an inverse variance-weighted mean of the psf-matched images of F200W, F277W, F356W, and F444W based on the F444W point-spread function (PSF). Source detection is conducted on the detection image, using `Photutils` (L. Bradley et al. 2025). As shown in Figure 1, since ID1 and ID2 have clumpy, complex structures, we conduct isophotal photometry in the detection images. We determine isophotal regions by setting two S/N ratio criteria for estimating photometric redshifts and stellar population of the galaxy. For photometric redshift estimates, to enhance the S/N ratios and get reliable SEDs, we adopt customized apertures, which are determined by regions 6σ above the background. To accurately estimate the stellar populations of the entire system, it is required to include faint diffuse fluxes that may come from older stars. We thus determine total isophotal apertures by regions 1.5σ above the background, which covers the entire system. We measure the flux of each filter with `Photutils`, adopting the customized and total isophotal apertures. To measure photometric uncertainties, we place the same customized and isophotal apertures on randomly selected sky regions and measure fluxes of the regions. We derive 1σ uncertainties from the 68% intervals of the resulting flux distributions. The customized aperture fluxes are corrected for total fluxes with a normalization factor obtained from total isophotal fluxes of the F277W filter. Note that we do not propagate the uncertainty of the normalization factor because it does not change the colors, which has negligible impacts on the photometric redshift estimates. For comparison, we also measure aperture photometry, extracted in circular apertures with diameters of $0\farcs3$ and corrected for total values with the Kron apertures (R. G. Kron 1980). In addition, the light that is missing beyond the Kron apertures is corrected in a similar method to that used in K. E. Whitaker et al. (2011) and J. R. Weaver et al. (2024). The measured photometry is presented in Table A1. The customized aperture fluxes and Kron fluxes are broadly consistent within the uncertainties while the total isophotal fluxes show slightly redder colors probably due to the inclusion of diffuse emission.

We measure UV slopes β of ID1 and ID2, using five filters of F200W, F210M, F277W, F300M, and F356W. Since F410M and F444W filters might be impacted by a Balmer break/jump (see Figure 2), we do not use them. The results yield relatively blue UV slopes of $\beta = -2.41 \pm 0.20$ for ID1 and $\beta = -2.60 \pm 0.23$ for ID2 (see Table 1).

2.3. Photometric Redshift

To derive photometric redshifts, we perform SED fitting to the customized aperture fluxes of ID1 and ID2 with `EAZY` (ver. 0.8.5; G. B. Brammer et al. 2008). We fit the blue SED templates of R. L. Larson et al. (2023), which are based on stellar population models of BPASS (J. J. Eldridge et al. 2017; E. R. Stanway & J. J. Eldridge 2018) and photoionization models of `Cloudy` (G. J. Ferland et al. 2017), and reflects blue UV slopes of observed galaxies at $z > 8$. We perform two sets of fitting, either including or excluding Lyα emission. For the models including Lyα emission, we apply absorption models of the intergalactic medium (IGM; A. K. Inoue et al. 2014). For the models without Lyα emission, we consider the additional Lyα damping wing absorption arising from the dense H I gas clouds in the circumgalactic medium (CGM), adopting the IGM + CGM absorption models (Y. Asada et al. 2025). While the hydrogen in the IGM is mostly neutral at $z > 10$, Lyα emission could still be observable if the galaxy hosts strong ionizing sources, such as faint systems with blue UV slopes that efficiently produce and leak ionizing photons (e.g., J. Witstok et al. 2025). We thus conduct SED fitting, considering the possible contribution of Lyα emission. We also perform `Prospector` (B. D. Johnson et al. 2021) SED fitting on the same photometry, as done with `EAZY`. We assume simple stellar populations (SSPs) with Flexible Stellar Population Synthesis (FSPS; C. Conroy & J. E. Gunn 2010), where we adopt the MIST isochrones (J. Choi et al. 2016) and MILES stellar library (P. Sánchez-Blázquez et al. 2006). Following B. Wang et al. (2024), the composite stellar populations (CSPs) are constructed with `Prospector-`β (B. Wang et al. 2023), where we assume the initial mass function (IMF) of G. Chabrier (2003), a two component dust model (S. Charlot & S. M. Fall 2000), and IGM absorption models of P. Madau (1995). As in `EAZY`, we either include or exclude Lyα emission. We adopt a flexible nonparametric star formation history (SFH) with seven logarithmically spaced time bins and a dynamic SFH prior, which depends on the

[74] https://dawn-cph.github.io/dja/

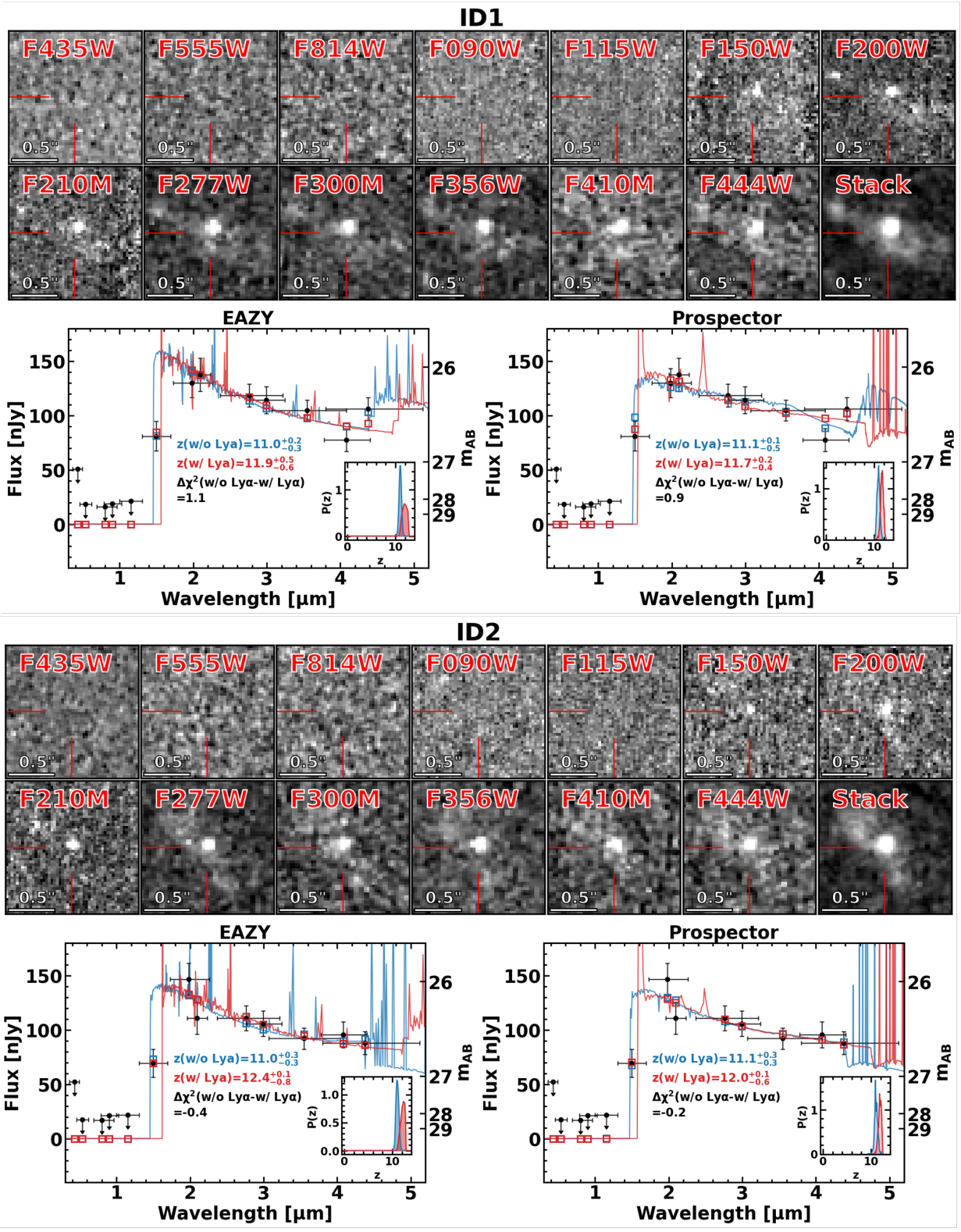


Figure 2. JWST + HST images and photometric redshift estimates for ID1 (top) and ID2 (bottom) of the Misty Moons. The upper panels show the $1\farcs5 \times 1\farcs5$ cutout images of 13 filters (F435W, F555W, F814W, F090W, F115W, F150W, F200W, F210M, F277W, F300M, F356W, F410M, and F444W) and stacked images of F200W, F277W, F356W, and F444W filters. The lower left and right panels present the results from `EAZY` and `Prospector` fitting, respectively. The black circles indicate the photometry measured from the customized apertures with its 1σ uncertainties (see Section 2.2) and wavelength coverages of the filters. For filters with nondetections, the 2σ upper limits are presented. The fluxes are normalized to total isophotal photometry with the F277W filter. The red curves (squares) indicate best-fit spectra (photometry) with no Lyα emission. The blue curves and squares are the same as the red ones, but with Lyα emission. The inset panels show the posterior probability distributions for redshifts.

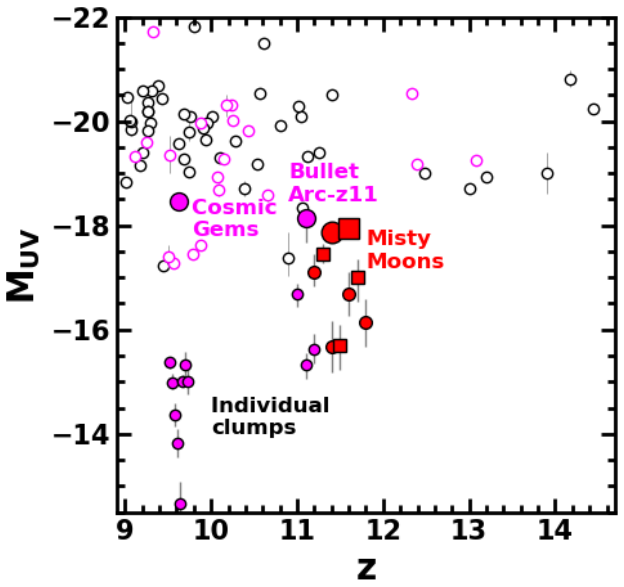


Figure 3. Absolute UV magnitude as a function of redshift. The red filled circles and squares indicate ID1 and ID2 of the Misty Moons ($z_{\rm phot} \sim 11$–12), respectively. The magenta filled circles represent highly magnified galaxies of the Cosmic Gems arc ($z_{\rm spec} = 9.63$; A. Adamo et al. 2024; L. D. Bradley et al. 2025; M. Messa et al. 2026) and BulletArc-z11 ($z_{\rm spec} = 11.10$; M. Bradač et al. 2025). The small filled symbols show the individual clumps of these galaxies. The magenta and black open circles denote the other spectroscopically confirmed $z > 9$ galaxies in lensing fields (T. Y.-Y. Hsiao et al. 2023, 2024; M. Stiavelli et al. 2023; H. Williams et al. 2023; M. Bradač et al. 2024; S. Fujimoto et al. 2024; C. Marconcini et al. 2024; D. J. McLeod et al. 2024; G. Roberts-Borsani et al. 2024; L. Napolitano et al. 2025; H. Yanagisawa et al. 2025) and blank fields (P. Arrabal Haro et al. 2023; A. J. Bunker et al. 2023; E. Curtis-Lake et al. 2023; S. Carniani et al. 2024; M. Castellano et al. 2024; F. D'Eugenio et al. 2024; K. N. Hainline et al. 2024; Y. Harikane et al. 2024; J. A. Zavala et al. 2024; V. Kokorev et al. 2025b; R. P. Naidu et al. 2026; L. Napolitano et al. 2025; S. Schouws et al. 2025; M. Tang et al. 2026; J. Witstok et al. 2025), respectively.

redshift and stellar mass, and reflects the cosmic SFR density (P. Behroozi et al. 2019). See B. Wang et al. 2023, 2024 for further details of the prior.

In Figure 2, we present the fitting results. The best-fit models excluding Lyα emission for both ID1 and ID2 yield redshifts of $z \sim 11$ while those including Lyα emission shifts the redshifts to $z \sim 12$. From the $\Delta\chi^2$ value for each fitting (see Figure 2), we cannot exclude either model including or excluding Lyα emission. In any case, the blue SEDs and nondetections in short-wavelength filters at <1.5 μm support a high probability of $P(z > 10) \sim 1.0$. We present the redshift and absolute UV magnitude distribution of $z > 9$ galaxies in Figure 3.

3. Lens Models

In this work, we construct two independent lens models, one with a revised version of the A. Zitrin et al. (2015) parametric method (a.k.a. Zitrin-Analytic; see L. J. Furtak et al. 2024 for more details), and Glafic (M. Oguri 2010, 2021). These lens models are constructed based on previously known multiple images (e.g., A. Zitrin et al. 2011) together with new identifications with NIRCam in the VENUS program, as shown in the colored circles in Figure 1. The predictions of the five multiple images (ID1–ID5) and their magnification values are broadly consistent among the two independent models. As described in Section 2.2, we identify two highly magnified counter images (ID1 and ID2) and a candidate for ID3. We do not detect ID4 and ID5, which is consistent with our model predictions of their low magnifications. We estimate the expected apparent magnitudes in F200W for ID4 and ID5 from that of ID1 and their magnification factors (Sections 3.1 and 3.2). The results are F200W $\sim$ 29 mag, which is $\sim$1 mag fainter than the 5σ detection limit of our NIRCam observations ($\sim$28 mag; Section 2.1). Further deep NIRCam imaging would be required to identify ID4 and ID5. We note that the geometry predicted by two independent lens models is similar to a hyperbolic umbilic (H-U) lensing configuration (e.g., M. Limousin et al. 2008; A. K. Meena & J. S. Bagla 2020; D. J. Lagattuta et al. 2023). This suggests that if all the five multiple images are confirmed, the presence of the H-U configuration could provide strong constraints on the radial profile of the lens. We detail the two models in the following sections.

3.1. Zitrin-Analytic (dPIE–PIEMD) Model

In this model, we include 10 sets of multiply imaged systems, including multiple knots in the three multiply imaged systems 1, 2, and 3 from A. Zitrin et al. (2011); the other less secure systems found by A. Zitrin et al. (2011) seem not to be true multiple image associations. Using MUSE data we determine the redshift of all three images of system 1 to be $z_{\rm spec} = 1.09$, which also spectroscopically confirms that all images are of the same system. We identify four new systems in JWST VENUS data, using also public data obtained by the SLICE program (PID: 5594; PI: Mahler): systems (6, 7, 8) and the Misty Moons system. We do not include the third multiple image candidate (ID3) for this system and only use the two clearly identified images (ID1&ID2) to constrain the model. Given its dropout nature, we set the redshift of the Misty Moons to be $z = 12$,[75] and system 1 to $z = 1.09$ and leave the redshifts of the other systems to be optimized by the model. The lens model is constructed using the so-called Zitrin-Analytic technique, which is a revised version of the A. Zitrin et al. (2015) parametric method (see also M. Pascale et al. 2022; L. J. Furtak et al. 2023 for more details). Cluster members are modeled as double Pseudo Isothermal Ellipsoids (dPIE; Á. Elíasdóttir et al. 2007) and the dark matter component of the cluster mass distribution is treated as a sum of diffused halos, modeled as pseudo isothermal elliptical mass distributions (PIEMDs; e.g., C. R. Keeton 2001). We find that one main dark matter halo centered on the main BCG but with the exact position free to move, is sufficient to well reproduce the lensing features in this cluster, but also add a second, smaller halo centered on the second BCG to improve its accuracy. We do not include here an external shear. The model reproduces all multiple images, with a χ^2 of 9.4 with 11 degrees of freedom (i.e., a reduced $\chi^2 \simeq 0.9$), and an rms of 0.″28. For the minimization, we first adopt a positional uncertainty of 0.″3, but for the final error and χ^2 calculation, we adopt the more commonly used positional uncertainty of 0.″5. For the Misty Moons, the model predicts three more images at R.A., decl.: (44.28487483, −23.43738994), (44.28650147, −23.43596856), and (44.28569941, −23.42626713). The calculated magnifications for ID1 and ID2 are 31^{+8}_{-1} and 35^{+2}_{-9}, and for the other three predicted images they are $30.4^{+3.6}_{-0.8}$, $6.9^{+1.6}_{-0.5}$, and $2.1^{+0.1}_{-0.1}$,

[75] Note that at this high source redshift the *exact* redshift has a negligible effect of the relative Dls/Ds ratio and thus, model.

Table 1
Properties of the Misty Moons

Name	R.A. (deg)	Decl. (deg)	$z_{\texttt{EAZY}}$	$z_{\texttt{EAZY+Ly}\alpha}$	$z_{\texttt{Prospector}}$	$z_{\texttt{Prospector+Ly}\alpha}$	$M_{\rm UV}$	β
ID1	⋯	⋯	$11.0^{+0.2}_{-0.3}$	$11.9^{+0.5}_{-0.6}$	$11.1^{+0.3}_{-0.3}$	$12.0^{+0.1}_{-0.6}$	$-17.90^{+0.15}_{-0.15}$	-2.41 ± 0.20
A.1	44.287102	−23.437968	⋯	⋯	⋯	⋯	$-17.12^{+0.28}_{-0.33}$	-2.60 ± 0.18
B.1	44.287275	−23.437903	⋯	⋯	⋯	⋯	$-15.66^{+0.35}_{-0.39}$	-1.83 ± 0.53
C.1	44.287029	−23.438028	⋯	⋯	⋯	⋯	$-16.70^{+0.32}_{-0.41}$	-3.47 ± 0.51
D.1	44.286927	−23.438012	⋯	⋯	⋯	⋯	$-16.13^{+0.43}_{-0.42}$	-2.71 ± 0.76
ID2	⋯	⋯	$11.0^{+0.3}_{-0.3}$	$12.4^{+0.1}_{-0.8}$	$11.1^{+0.3}_{-0.3}$	$12.0^{+0.1}_{-0.6}$	$-17.93^{+0.18}_{-0.19}$	-2.60 ± 0.23
A.2	44.288122	−23.437200	⋯	⋯	⋯	⋯	$-17.46^{+0.15}_{-0.17}$	-2.94 ± 0.15
B.2	44.288080	−23.437306	⋯	⋯	⋯	⋯	$-15.70^{+0.47}_{-0.38}$	-1.99 ± 0.77
C.2	44.288215	−23.437158	⋯	⋯	⋯	⋯	$-17.00^{+0.26}_{-0.25}$	-2.80 ± 0.61

Note. Photometric redshifts are measured for customized aperture fluxes of ID1 and ID2, using `EAZY` and `Prospector`. We present two types of redshifts, one of which is based on SED models without Lyα emission ($z_{\texttt{EAZY}}$ and $z_{\texttt{Prospector}}$), while the other is based on SED models with Lyα emission ($z_{\texttt{EAZY+Ly}\alpha}$ and $z_{\texttt{Prospector+Ly}\alpha}$). The $M_{\rm UV}$ values are corrected for magnification.

respectively. The third image at (R.A., decl.) = (44.28487483, −23.43738994) is a bit apart from the candidate for ID3, shown in Figure 1, and the magnification factor is thus deviated from that for the candidate of ID3 predicted by the Glafic model (Section 3.2). The magnification derived with the Zitrin-Analytic model at the position of the candidate of ID3 is $12.7^{+2.8}_{-0.2}$, which is comparable to that estimated with the Glafic model (Section 3.2).

3.2. Glafic Model

We include three multiple image systems identified in A. Zitrin et al. (2011) as well as three additional multiple image systems identified in the VENUS data including the Misty Moons as observational constraints. For the Misty Moons, in addition to ID1 and ID2, the position of the ID3 candidate at (44.2845714, −23.4367132) is also included. We model the mass distribution assuming a Navarro–Frenk–White (NFW; J. F. Navarro et al. 1996) profile for the halo component and member galaxy perturbations modeled by pseudo-Jaffe ellipsoids. In addition, the external shear is included. Since no spectroscopic redshift is available for all these multiple image systems except system 1, we include their photometric redshift as priors. Assuming the positional error of 0.″4, our best-fitting model has $\chi^2 = 14.7$ for the degree of freedom of 15. The rms between model-predicted and observed multiple image positions is 0.″36. The model predicts the magnification of ID1 of 28 ± 3, ID2 of 21 ± 3, and ID3 of 11 ± 1. It also predicts additional images (ID4, ID5) at around (44.2862877, −23.4354116) and (44.2848497, −23.4255854), with their magnifications of 2.4 ± 1.3 and 2.6 ± 0.2, respectively. Their low magnifications well explain the nondetection in the VENUS data.

4. Analysis

4.1. Clump Detection

We conduct clump identification, following previous studies (e.g., C. J. Conselice et al. 2003; A. Calabrò et al. 2019; B. S. Kalita et al. 2024). We use the detection image constructed from F200W, F277W, F356W, and F444W filter images (see Section 2.2) and smooth it, using a Gaussian kernel with a standard deviation of $\sigma = 6$ pixel. The smoothed image is subtracted from the original image, leaving behind a contrast map. We perform source extraction in the contrast map with a threshold of S/N = 2, using `Photutils` (L. Bradley et al. 2025), and identify four clumps (A.1, B.1, C.1, and D.1) for ID1 and three clumps (A.2, B.2, and C.2) for ID2 (see Figure 4), which are detected in almost all filters at >1.5 μm. In Figure 5, we compare image-plane and source-plane images of ID1 and ID2. The source-plane images are reconstructed pixel-by-pixel with the Glafic model. Despite the lensing distortions, the reconstructed morphologies and relative positions are highly similar, suggesting that the individual clumps of ID1 and ID2 may correspond to the same intrinsic structures.

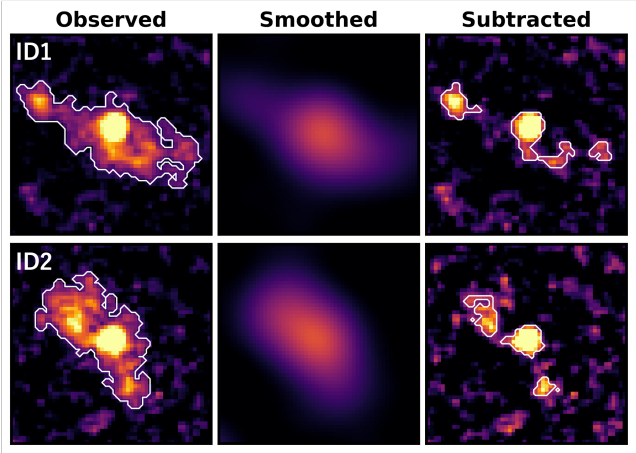


Figure 4. Clump detection procedure for ID1 and ID2. From left to right, each panel presents the observed detection images (F200W + F277W + F356W + F444W), smoothed-host images, and host-subtracted contrast images (Section 4.1). The white contours in the left and right panels indicate isophotal regions detected with `Photutils`.

4.2. Clump Modeling

To simultaneously model the multiple clumps, we conduct Sérsic-profile fitting using `GALFIT` (C. Y. Peng et al. 2010). For ID1, we adopt a five-component model consisting of five Sérsic profiles to simultaneously fit the four individual clumps and diffuse light. In a similar way, a four-component model consisting of four Sérsic profiles is used for ID2. We set the initial parameters of the fitting with the clump identification results with `Photutils` described in the previous section.

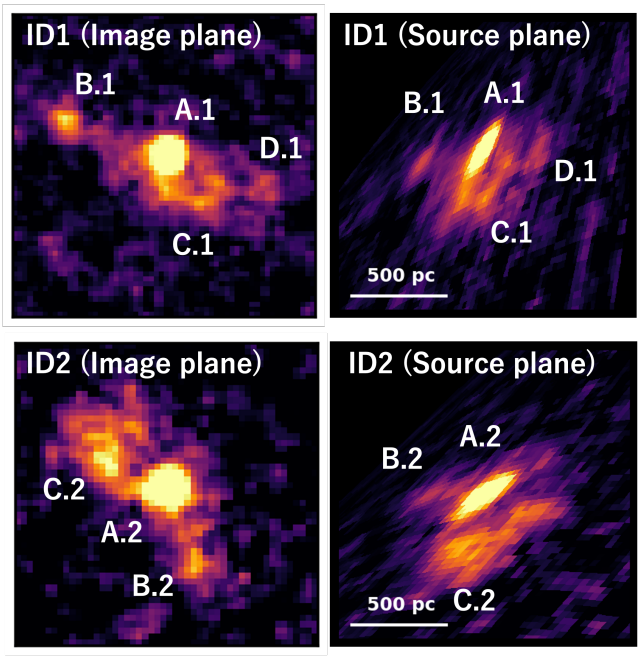


Figure 5. Detection images (F200W + F277W + F356W + 444W) of ID1 and ID2 in the image plane (left) and source plane (right).

We fix the Sérsic index to $n = 1$ for the individual clumps except for the diffuse light, and set the boundary limits of the other parameters in the same manner as S. Fujimoto et al. (2025). We fit to the detection images because of their higher S/N ratios than the individual filter images. The best-fit models and residuals of ID1 and ID2 are presented in Figure 6. The intrinsic half-light radius in the source plane, $r_{\rm eff,int}$, is obtained by dividing the measured half-light radius in the image plane by the square root of the magnification factor predicted by the Glafic model. The most compact clumps of A.1 and A.2 are only marginally larger than the PSF in the detection images, leaving modest residuals after pure-PSF fitting. To further investigate whether these clumps are spatially resolved, we additionally analyze the F200W images, which have a smaller PSF and therefore provide higher spatial resolution. In the F200W images, the clumps are well reproduced by the PSF without significant residuals, suggesting that they may be unresolved. The similarly point-like appearance of these clumps across multiple images is also consistent with the unresolved interpretation. The corresponding radial surface-brightness profiles are presented in Figure B1. If these clumps are unresolved, we adopt half width at half maximum of the PSF (0.″05) as an upper limit of the observed effective radius. The corresponding upper limit of the intrinsic effective radius is estimated by dividing the observed one by the tangential magnification ($\mu_{\rm tan} = 10.1$ for A.1 and 7.7 for A.2). The apparent discrepancy between the detection and F200W images can be interpreted as follows. If these clumps are marginally resolved, the low S/N ratio of the F200W images may prevent detection of the low-surface-brightness outskirts of the clumps, causing them to appear PSF-like. Alternatively, if these clumps are unresolved, the slightly extended appearance in the detection images may arise from residual contamination by the diffuse component and correlated noise. Because the current data do not allow us to distinguish between these two scenarios, we report both the best-fit effective radii assuming marginally resolved clumps and upper limits assuming unresolved clumps in Table 2.

We measure the clump fluxes by fitting the same models as used for the $r_{\rm eff}$ measurement to the PSF-matched filter images. We set only the fluxes as free parameters, and fix the other parameters of the Sérsic profiles to the best-fit ones obtained from the detection images. To derive the flux uncertainties, we conduct Monte Carlo simulations. We construct mock observation images by injecting the PSF convolved best-fit models to randomly selected sky regions with no other sources. We perform identical flux measurements with the mock observation images and determine the 1σ uncertainties from the 68% intervals of the resulting flux distributions.

4.3. SED Fitting

To derive stellar populations of the entire systems and all clumps of ID1 and ID2, we conduct SED fitting using `Prospector` with flexible nonparametric SFHs in the same way as described in Section 2.3. To focus on the stellar population properties, we fix the redshift to be $z = 11.5$, which is a mean value of all the photometric redshifts presented in Table 1. We use total isophotal fluxes for the entire systems of ID1 and ID2. For comparison of clump stellar populations, we also perform `Bagpipes` (A. C. Carnall et al. 2018) SED fitting with short SFHs, which is conducted for high-z star-forming clumps (E. Vanzella et al. 2022; A. Adamo et al. 2024; L. D. Bradley et al. 2025; A. Claeyssens et al. 2025; S. Fujimoto et al. 2025). We adopt SPS models by G. Bruzual & S. Charlot (2003) and include nebular emission calculated with `Cloudy`. We fix the redshift to be $z = 11.5$, same as `Prospector` fitting, and assume a D. Calzetti et al. (2000) attenuation law. For SFHs, we assume delayed-τ models, expressed as SFR $\propto te^{-t/\tau}$, where we adopt a short timescale of $\tau = 10$ Myr, following the studies of high-z clumps/star clusters (e.g., A. Adamo et al. 2024; A. Claeyssens et al. 2025). We adopt flat priors for formed mass $5 < \log(M_*/M_\odot) < 13$, formed age $1\,{\rm Myr} < t < 1\,{\rm Gyr}$, formed metallicity $0.01 < Z_*/Z_\odot < 1$, V-band extinction $0 < A_{\rm V} < 3$, and ionization parameter $-3 < \log(U) < -1$. In Table 3, we present the inferred properties from the SED fitting.

5. Results and Discussion

5.1. Physical Properties

The entire systems of ID1 and ID2 have intrinsically faint UV luminosity $M_{\rm UV} = -17.9 \pm 0.2$, which corresponds to sub-L_* (Y. Harikane et al. 2023), placing them among the faintest galaxies known at $z > 10$ (see Figure 3). The intrinsic stellar mass and half-light radius of ID1 (ID2) are $\log M_{*,\rm int} = 3.7^{+3.0}_{-1.7} \times 10^7\,M_\odot$ ($3.4^{+2.2}_{-1.7} \times 10^7\,M_\odot$) and $\rm r_{eff,int} = 181 \pm 18$ pc (197 ± 28 pc), respectively. We estimate the half-light radii of ID1 and ID2 from the growth curve of their detection images (see Figure 5). We then obtain the intrinsic half-light radii by correcting for magnification with the Glafic model. We note that the choice of the models has minor effects on the stellar mass and half-light radius estimates, as demonstrated in Appendix C. The sizes and UV luminosities of ID1 and ID2 are comparable to the size–UV luminosity relation for $z > 10$ (Y. Ono et al. 2025), which suggests that our galaxy is a representative example of faint, low-mass galaxies at $z > 10$. As mentioned above, a remarkable feature of this galaxy is that

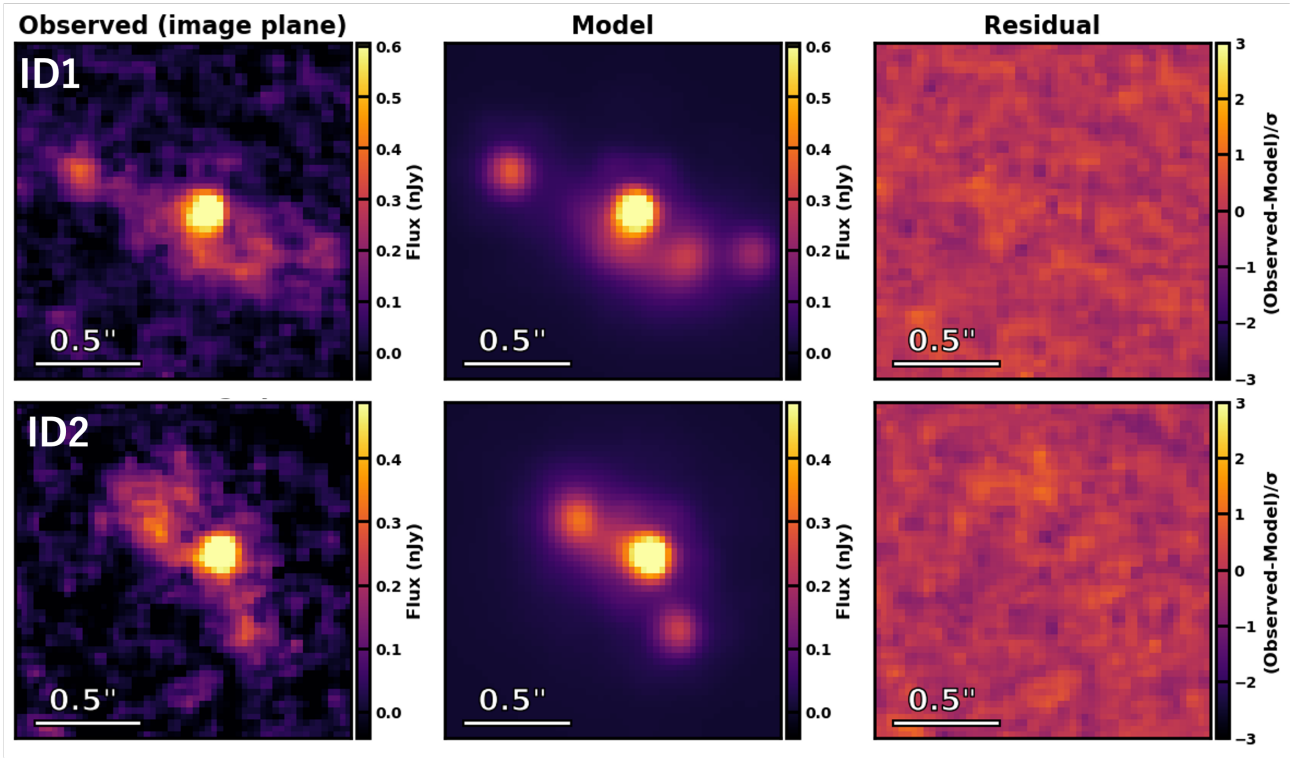


Figure 6. Clump modeling results for ID1 and ID2 of the Misty Moons system. From left to right, the 1.″5 × 1.″5 observed images, best-fit model images, and residual images divided by the 1σ error maps are presented.

Table 2
Properties of the Misty Moons (continued)

Name	$\log(M_{*,\rm int})$ ($M_\odot$)	$r_{\rm eff}$ (pc)	$r_{\rm eff,int}$ (pc)	$\log(\Sigma_*)$ ($M_\odot$ pc^{-2})	$\log(\Sigma_{\rm SFR})$ ($M_\odot$ yr^{-1} kpc^{-2})	$\mu_{\rm Zitrin-Analytic}$	$\mu_{\rm Glafic}$
ID1	7.57 ± 0.26	958 ± 78	181 ± 18	2.25 ± 0.27	0.46 ± 0.11	$31.0^{+8.0}_{-1.0}$	$28.0^{+3.0}_{-3.0}$
A.1	7.03 ± 0.19	83 ± 11[a]	15 ± 3[a]	3.88 ± 0.19[a]	2.24 ± 0.13[a]	$30.6^{+1.8}_{-6.7}$	$30.8^{+8.1}_{-7.8}$
		<203[b]	<20[b]	>3.62[b]	>1.97[b]		
B.1	7.09 ± 0.41	134 ± 24	22 ± 5	3.59 ± 0.41	1.83 ± 0.37	$29.6^{+1.6}_{-6.7}$	$37.4^{+11.2}_{-10.3}$
C.1	6.87 ± 0.24	347 ± 34	67 ± 12	2.40 ± 0.23	0.66 ± 0.16	$33.9^{+1.6}_{-8.4}$	$27.0^{+8.1}_{-6.4}$
D.1	6.92 ± 0.36	189 ± 39	36 ± 8	3.02 ± 0.38	1.19 ± 0.33	$40.6^{+2.9}_{-11.2}$	$27.4^{+6.8}_{-6.4}$
ID2	7.53 ± 0.22	903 ± 116	197 ± 28	2.15 ± 0.24	0.45 ± 0.14	$35.0^{+2.0}_{-9.0}$	$21.0^{+3.0}_{-3.0}$
A.2	7.02 ± 0.14	83 ± 42[a]	17 ± 9[a]	3.72 ± 0.51[a]	2.18 ± 0.47[a]	$31.0^{+7.2}_{-0.6}$	$21.4^{+2.8}_{-3.0}$
		<203[b]	<26.4[b]	>3.38[b]	>1.84[b]		
B.2	7.11 ± 0.35	147 ± 145	36 ± 33	3.24 ± 0.86	1.28 ± 0.85	$40.2^{+14.1}_{-0.9}$	$28.3^{+3.7}_{-3.9}$
C.2	6.98 ± 0.24	296 ± 111	56 ± 21	2.74 ± 0.46	0.98 ± 0.39	$26.6^{+4.9}_{-0.5}$	$18.6^{+2.5}_{-2.4}$

Notes. The $M_{*,\rm int}$ and $r_{\rm eff,int}$ values are corrected for magnification while the $r_{\rm eff}$ values are measured in the image plane. We derive $\Sigma_{\rm SFR}$ values, using the SFRs in the recent 10 Myr derived from `Prospector` SED fitting.
[a] The size and surface density measurements from detection images where these clumps are marginally resolved.
[b] The size and surface density limits from F200W images where these clumps are unresolved (see Section 4.2).

due to the strong magnification, it is resolved into multiple clumps, the central one of which is more than 2 times brighter than the other clumps. At $z > 10$, there exist a few studies about similar clumpy galaxies, BulletArc-z11 ($z_{\rm spec} = 11.10$; M. Bradač et al. 2025) and MACS0647-JD ($z_{\rm spec} = 10.17$; T. Y.-Y. Hsiao et al. 2023, 2024), both of which show a bright central clump and the other smaller clumps. Interestingly, MACS0647-JD may be undergoing a galaxy merger based on the different SFHs among the clumps while the individual clumps of BulletArc-z11 exhibit similar SFHs. We further discuss the possible clump formation scenario in the next section.

In the left panel of Figure 7, we present the size and stellar mass relation of local star clusters, star-forming clumps, and dwarf galaxies. The individual clumps of the Misty Moons are located in similar regions to local nuclear star clusters (NSCs), young massive star clusters (YMCs), ultracompact dwarfs (UCDs), and compact elliptical galaxies (cEs; M. A. Norris et al. 2014) as well as high-z individual star-forming clumps of the BulletArc-z11 ($z_{\rm spec} = 11.10$; M. Bradač et al. 2025) and

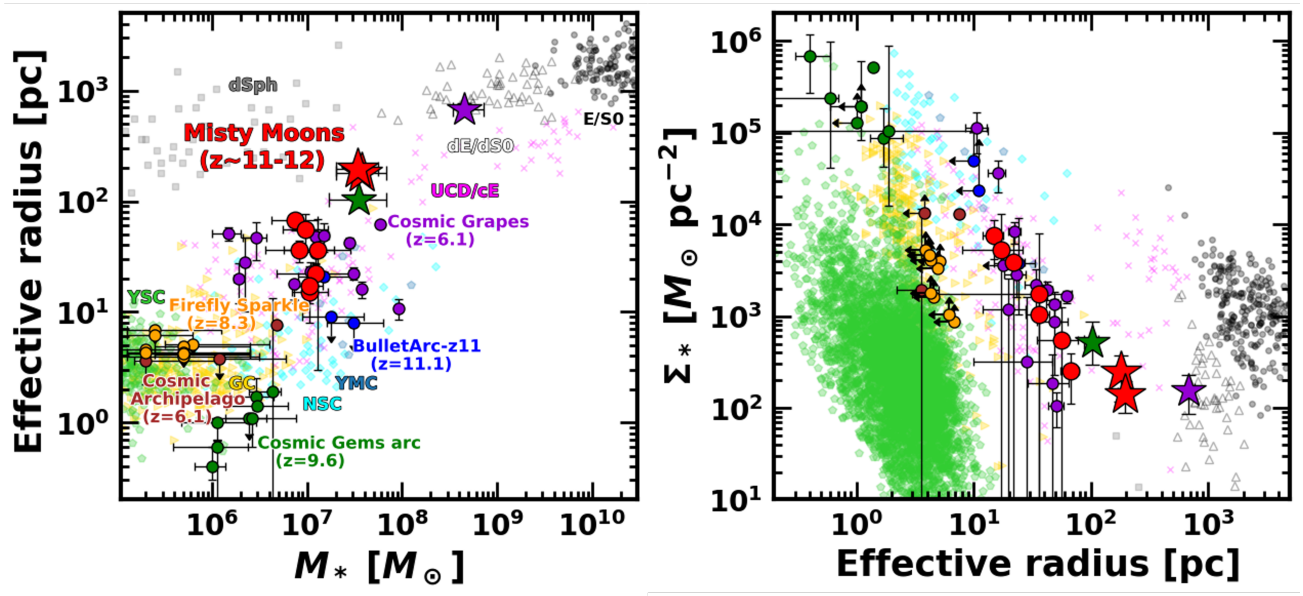


Figure 7. Physical properties of individual clumps. Left: stellar mass vs. effective radius relation. Right: stellar mass surface density as a function of effective radius. The star symbols indicate the entire systems while the circles are individual clumps. The red, blue, green, orange, brown, and purple symbols show the Misty Moons ($z_{\rm phot} \sim 11$–12; This work), BulletArc-z11 ($z_{\rm spec}$11.10; M. Bradač et al. 2025), Cosmic Gems arc ($z_{\rm spec} = 9.63$; A. Adamo et al. 2024; L. D. Bradley et al. 2025; M. Messa et al. 2026; E. Vanzella et al. 2026, Firefly Sparkle ($z_{\rm spec} = 8.27$; L. Mowla et al. 2024), Cosmic Archipelago ($z_{\rm spec} = 6.14$; M. Messa et al. 2025), and Cosmic Grapes ($z_{\rm spec} = 6.07$; S. Fujimoto et al. 2025), respectively. For comparison, the other symbols represent local galaxies or star clusters of elliptical/S0 galaxies (E/S0; gray circles), dwarf elliptic/S0 galaxies (dEs/dS0; open triangles), dwarf spheroids (dSph; gray squares), ultracompact dwarfs/compact elliptical galaxies (UCD/cE; magenta crosses), young massive star clusters (YMC; blue pentagon), nuclear star clusters (NSCs; cyan diamonds), globular clusters (GC; yellow triangles), and young star clusters (YSC; green pentagon) taken from the compilation in M. A. Norris et al. (2014).

Table 3
Physical Properties of the Misty Moons in the Image Plane Estimated from SED Fitting

Name	$\log(\mu M_*)$ ($M_\odot$)	Age (Myr)	A_V (mag)	μSFR (10 Myr) ($M_\odot$ yr^{-1})	μSFR (100 Myr) ($M_\odot$ yr^{-1})
`Prospector`, flexible nonparametric SFH					
ID1	$9.01^{+0.19}_{-0.24}$	$62.1^{+41.7}_{-28.0}$	$0.02^{+0.04}_{-0.02}$	$16.9^{+3.3}_{-3.4}$	$9.0^{+2.0}_{-2.8}$
A.1	$8.50^{+0.15}_{-0.15}$	$42.4^{+26.5}_{-19.2}$	$0.02^{+0.03}_{-0.01}$	$7.4^{+1.2}_{-1.0}$	$3.2^{+1.2}_{-0.9}$
B.1	$8.64^{+0.44}_{-0.33}$	$56.1^{+44.2}_{-27.3}$	$0.24^{+0.49}_{-0.16}$	$6.8^{+9.7}_{-2.9}$	$3.9^{+6.7}_{-1.9}$
C.1	$8.28^{+0.25}_{-0.19}$	$54.2^{+34.2}_{-26.2}$	$0.03^{+0.06}_{-0.02}$	$3.6^{+1.1}_{-0.8}$	$1.9^{+1.1}_{-0.6}$
D.1	$8.36^{+0.42}_{-0.27}$	$66.7^{+44.1}_{-33.4}$	$0.14^{+0.27}_{-0.10}$	$3.4^{+3.0}_{-1.2}$	$2.1^{+2.4}_{-0.9}$
ID2	$8.86^{+0.22}_{-0.19}$	$58.5^{+40.0}_{-28.2}$	$0.02^{+0.03}_{-0.02}$	$14.5^{+2.4}_{-2.4}$	$6.8^{+2.5}_{-2.0}$
A.2	$8.35^{+0.16}_{-0.10}$	$35.9^{+21.7}_{-14.5}$	$0.01^{+0.01}_{-0.00}$	$6.5^{+0.6}_{-0.6}$	$2.4^{+0.8}_{-0.5}$
B.2	$8.34^{+0.4}_{-0.3}$	$62.6^{+47.5}_{-30.1}$	$0.14^{+0.25}_{-0.10}$	$3.1^{+2.6}_{-1.1}$	$1.9^{+2.3}_{-0.8}$
C.2	$8.45^{+0.32}_{-0.22}$	$64.7^{+47.0}_{-33.2}$	$0.06^{+0.12}_{-0.05}$	$4.9^{+1.8}_{-1.3}$	$2.6^{+1.8}_{-0.9}$
`Bagpipes`, delayed-τ ($\tau = 10$ Myr) SFH					
Name	$\log(\mu M_*)$ ($M_\odot$)	Age (Myr)	A_V (mag)	μSFR ($M_\odot$ yr^{-1})	
A.1	$8.51^{+0.36}_{-0.30}$	$15.6^{+15.0}_{-9.7}$	$0.06^{+0.08}_{-0.04}$	$3.8^{+5.4}_{-2.1}$	
B.1	$9.05^{+0.32}_{-0.59}$	$42.6^{+46.1}_{-32.7}$	$0.48^{+0.39}_{-0.33}$	$10.3^{+11.8}_{-8.0}$	
C.1	$8.27^{+0.43}_{-0.40}$	$18.2^{+19.9}_{-12.5}$	$0.08^{+0.12}_{-0.06}$	$2.2^{+4.2}_{-1.4}$	
D.1	$8.66^{+0.58}_{-0.62}$	$32.1^{+49.8}_{-23.4}$	$0.31^{+0.44}_{-0.23}$	$4.0^{+10.0}_{-3.1}$	
A.2	$8.71^{+0.28}_{-0.36}$	$26.7^{+14.5}_{-13.5}$	$0.03^{+0.05}_{-0.02}$	$6.3^{+6.1}_{-3.7}$	
B.2	$8.54^{+0.50}_{-0.55}$	$27.9^{+39.1}_{-19.4}$	$0.30^{+0.39}_{-0.21}$	$3.5^{+7.2}_{-2.6}$	
C.2	$8.63^{+0.49}_{-0.53}$	$25.0^{+33.7}_{-17.9}$	$0.18^{+0.23}_{-0.13}$	$4.8^{+10.1}_{-3.5}$	

Note. For the entire systems (ID1 and ID2), we use isophotal fluxes and fit only with `Prospector`. Stellar masses and SFRs are not corrected for magnification.

Cosmic Grapes ($z_{\rm spec} = 6.07$; S. Fujimoto et al. 2025). The Cosmic Gems arc ($z_{\rm spec} = 9.63$; A. Adamo et al. 2024; M. Bradač et al. 2024; M. Messa et al. 2026; E. Vanzella et al. 2026) and Firefly Sparkle ($z_{\rm spec} = 8.30$L. Mowla et al. 2024) are further resolved into <10 pc scale star clusters, similar to local young star clusters (YSCs) and GCs. The studies of GCs in galaxy clusters at $z \sim 0.3$–0.9 have become rather robust with JWST/NIRCam (see J. M. Berkheimer et al. 2026; W. E. Harris et al. 2025). The formation ages and masses of these low-z GCs estimated from their colors are broadly consistent with those of our clumps, suggesting the possibility of being proto-GCs. We note that GCs are predicted to lose a large fraction of stars over time due to tidal friction in their host galaxies (e.g., W. E. Harris et al. 2025), likely explaining why local GCs have systematically lower stellar masses. Combining the delensed stellar masses and SFRs with intrinsic half-light radii, we derive the stellar mass and SFR surface densities. Some of the clumps show high surface densities of $\Sigma_* \sim 10^4\,M_\odot\,{\rm pc}^{-2}$ and $\Sigma_{\rm SFR} \sim 10^2\,M_\odot\,{\rm yr}^{-1}\,{\rm kpc}^{-2}$. For the most compact clumps of A.1 and A.2, if they are unresolved, the surface densities may be even higher (see Section 4.2). These values are comparable to those of compact, nitrogen-rich galaxies at $z \gtrsim 6$ (e.g., Y. Isobe et al. 2023a; M. Castellano et al. 2024; P. Senchyna et al. 2024; D. Schaerer et al. 2024) although similarly high densities can also be found in a few non-nitrogen-rich galaxies (D. Schaerer et al. 2024).

As presented in Table 3, `Prospector` fitting results indicate that most of the clumps consist of young (∼40–70 Myr) stars, formed in a low-dust ($A_V \lesssim 0.1$ mag) environment. This is consistent with the rising star formation history obtained for these clumps, which is likely more common in the high-redshift Universe (e.g., Y. Harikane et al. 2025; M. Tang et al. 2026). The results from `Bagpipes` are broadly

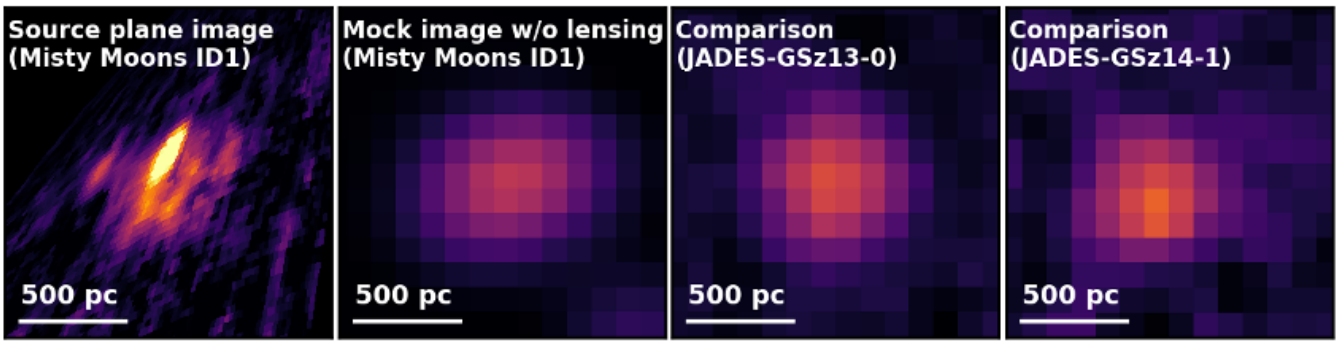


Figure 8. Comparison of the morphology of faint galaxies with and without lensing magnification. The leftmost panel presents the source-plane image for ID1 of the Misty Moons. The second panel shows the mock image convolved with the NIRCam PSF. The third and rightmost figures represent the images of faint galaxies, GS-z13-0 ($z_{\rm spec} = 13.20$; E. Curtis-Lake et al. 2023) and GS-z14-1 ($z_{\rm spec} = 13.90$; S. Carniani et al. 2024). Without lensing magnification, ID1, GS-z13-0, and GS-z14-1 exhibit similar morphologies.

consistent with those from `Prospector`. The stellar ages for individual clumps estimated with nonparametric SFHs are relatively older than those estimated with short SFHs, although the differences are not conclusive given their uncertainties. If real, these differences may indicate that individual clumps contain older stellar populations. We cannot yet exclude the possibility that the central clumps (A.1 and A.2) host active galactic nuclei (AGNs), given their brightness (about half of the galaxy's total brightness) and compactness, while we note that they may be marginally resolved with respect to the PSF (see Section 4.2).

5.2. Clump Formation

As shown in Figure 5, multiple clumps are resolved in the Misty Moons at this high redshift due to the high magnifications. To investigate the lensing effects, we construct a mock observation image of ID1 by convolving the source-plane image with the NIRCam PSF. The mock image shows smoothed morphology, yielding a light distribution comparable to that of similarly faint ($M_{\rm UV} \gtrsim -19$) galaxies at $z > 10$, GS-z13-0 ($z_{\rm spec} = 13.20$; E. Curtis-Lake et al. 2023) and GS-z14-1 ($z_{\rm spec} = 13.90$; S. Carniani et al. 2024), as shown in Figure 8. These resolution-dependent effects have also been reported in mock observations of galaxies from zoom-in cosmological simulations, where galaxy substructures identified at high spatial resolution become blended or undetectable when observed at lower resolution (e.g., A. Zanella et al. 2021). As discussed for similarly strongly lensed galaxies at $z \gtrsim 6$ (S. Fujimoto et al. 2025; E. Vanzella et al. 2026), this suggests that faint galaxies at $z > 10$ likely have internal clumpy structure that remains unresolved without lensing magnifications.

To evaluate clumpiness in the Misty Moons, we derive the clumpiness parameter S and clump luminosity function (LF), following S. Fujimoto et al. (2025). The clumpiness parameter is defined as

$$S = 10 \times \Sigma_{x,y=1,1}^{N,N} \frac{(I_{x,y} - I_{x,y}^{\sigma}) - (B_{x,y} - B_{x,y}^{\sigma})}{I_{x,y}}, \quad (1)$$

where $I_{x,y}$ is the sky-subtracted flux values of the galaxy at position (x, y), $I_{x,y}^{\sigma}$ is the flux values of the galaxy at position (x, y) smoothed by Gaussian kernel with width σ, $B_{x,y}$ and $B_{x,y}^{\sigma}$ are the unsmoothed and smoothed flux values, respectively, but for background pixels in an area equal to that of the galaxy, and N is the size of the galaxy in pixels (C. J. Conselice et al. 2003). To ensure sufficient S/N ratios in individual pixels, we use the detection image of ID1 (Section 4.1) within a circular aperture of radius $r = 0\farcs7$ centered on the peak pixel and adopt $\sigma = 0\farcs2$, following S. Fujimoto et al. (2025). We confirm that these values are well matched to the observed light distribution of ID1. The 1σ uncertainty of the S value is derived from 1000 Monte Carlo realizations of the observed image, where each pixel is perturbed according to its 1σ uncertainty assuming a Gaussian error distribution. We obtain $S = 0.69^{+0.16}_{-0.17}$ for the Misty Moons, which is comparable to the high value measure for the Cosmic Grapes at $z = 6.1$ (S. Fujimoto et al. 2025; left panel of Figure 9). In the right panel, we present the cumulative clump LF as a function of SFR normalized by the galaxy stellar mass, allowing comparison among galaxies with different stellar masses. We calculate the number of clumps in the Misty Moons within each SFR bin using the SED-based SFRs, adopting the mean value of ID1 and ID2. We derive 1σ uncertainty based on the Poisson statistics (e.g., N. Gehrels 1986). The clump LF of the Misty Moons is systematically higher than those of lensed galaxies at $z \sim 1$–3 (R. C. Livermore et al. 2015) and Cosmic Grapes ($z = 6.1$). We further compare the clumpiness parameter and clump LF with those of simulated galaxies at $z \sim 6$–8 analyzed by S. Fujimoto et al. (2025), based on the cosmological zoom-in simulations of SERRA (A. Pallottini et al. 2022), TNG50[76] (A. Pillepich et al. 2019), and FIRE[77] (A. Wetzel et al. 2023). As described in S. Fujimoto et al. (2025), the selected SERRA, TNG50, and FIRE galaxies show gas kinematics with likely rotating disk, asymmetric velocity gradient, and disturbed gas without major mergers, respectively. The Misty Moons exhibit higher clumpiness than these simulated galaxies in both the S values and clump LFs, similar to the Cosmic Grapes. For the Cosmic Grapes, one plausible explanation for the numerous clumps despite the presence of a rotating disk is substantially weak feedback (S. Fujimoto et al. 2025). Although whether a rotating disk exists in the Misty Moons cannot be confirmed with the current data, the weak feedback scenario may still be applicable to the Misty Moons

[76] https://www.tng-project.org/about/
[77] https://flathub.flatironinstitute.org/fire

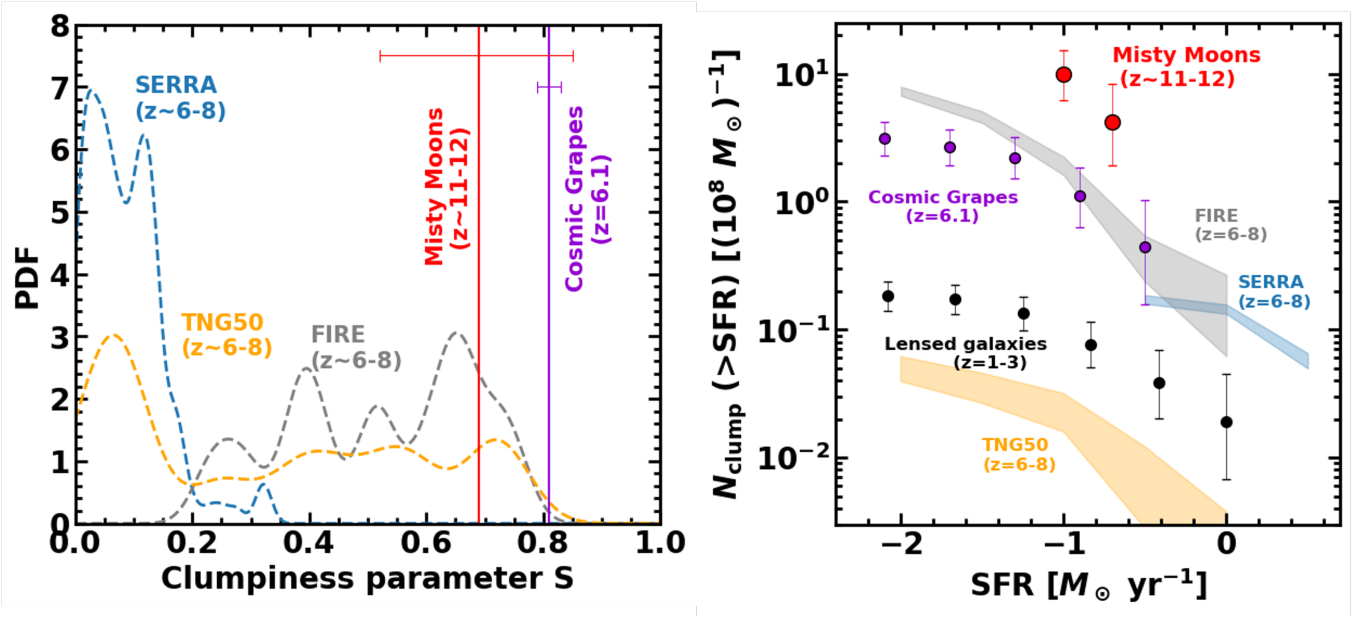


Figure 9. Left: probability distributions of clumpiness parameters S. The red vertical and horizontal lines indicate the S measurement and its 1σ uncertainty of the Misty Moons at $z \sim 11$–12, respectively, while the purple lines show those for the Cosmic Grapes at $z = 6.1$ (S. Fujimoto et al. 2025). The blue, yellow, and gray dashed curves show the distributions of the S measurements for galaxies in the SERRA (A. Pallottini et al. 2022), TNG50 (A. Pillepich et al. 2019), and FIRE (A. Wetzel et al. 2023) simulations at $z \sim 6$–8, respectively, obtained by S. Fujimoto et al. (2025). Right: cumulative clump luminosity function normalized by galaxy stellar mass as a function of clump star formation rate. The red, purple, and black circles present the measurements for the Misty Moons, Cosmic Grapes, and lensed galaxies at $z \sim 1$–3 (R. C. Livermore et al. 2015), respectively. The blue, yellow, and gray shaded regions denote the measurements for the SERRA, TNG50, and FIRE galaxies, respectively.

as well, given its high clumpiness comparable to that of the Cosmic Grapes. The comparisons of the clumpiness among the observed and simulated galaxies across cosmic time suggest that the galaxies at higher redshift tend to be more clumpy, which is consistent with the observations of many clumpy galaxies at $z > 6$ (e.g., A. Adamo et al. 2024; L. D. Bradley et al. 2025; L. Mowla et al. 2024; M. Bradač et al. 2025; S. Fujimoto et al. 2025; Y. Harikane et al. 2025; M. Messa et al. 2025, 2026; E. Vanzella et al. 2026). The elevated clumpiness is qualitatively consistent with a large fraction of star formation being concentrated in compact clumps, motivating a direct examination of the clustered stellar mass fraction.

In the left panel of Figure 10, we compare the clustered mass fractions of high-z galaxies (colored symbols; E. Vanzella et al. 2022; A. Adamo et al. 2024; L. D. Bradley et al. 2025; M. Bradač et al. 2025; A. Claeyssens et al. 2025; S. Fujimoto et al. 2025; M. Messa et al. 2026; E. Vanzella et al. 2026; this work) with cluster mass fractions of local galaxies (gray symbols; blue compact dwarfs (BCDs): G. Östlin et al. 2001; A. Adamo et al. 2011 and low-mass dwarfs: D. Calzetti et al. 2015; D. O. Cook et al. 2023). We derive the clustered mass fraction, dividing the sum of the clump/cluster masses by total galaxy mass. For the Misty Moons, the probability distributions of the mass fractions pile up near unity. We thus obtain 1σ lower limits of 90% for ID1 and 78% for ID2, using the total stellar masses derived from the total isophotal fluxes. While the isophotal regions include light from a diffuse component that may contain older stellar populations, this contribution could be overwhelmed by the light from young star-forming clumps, which is known as stellar outshining (e.g., D. Narayanan et al. 2024). Since the stellar outshining may lead to an underestimate of the total stellar mass, we also derive the clump mass fractions of the Misty Moons, using diffuse fluxes explicitly estimated from the `Galfit` fitting (Section 4.2). The resulting clump mass fractions are 54^{+42}_{-24}% for ID1 and 44^{+38}_{-23}% for ID2. The differences of the estimates from those derived with the total isophotal fluxes are within a factor of 2, which does not change our conclusion based on differences by orders of magnitude. In the following discussion, we adopt the mass fractions based on the total isophotal fluxes as fiducial results of the Misty Moons because the stellar masses estimated from the diffuse fluxes have larger uncertainties due to their low surface brightnesses. For the cluster mass fractions of the Cook et al. sample, we first calculate cluster masses by multiplying cluster formation rate of CFR (1–100 Myr) in Table 4 of D. O. Cook et al. (2023) by 100 Myr. We then obtain the cluster mass fractions, dividing the cluster masses by total masses presented in D. Calzetti et al. (2015). Similarly, we derive the mass fraction of luminous BCDs (Haro11 and ESO338) from A. Adamo et al. (2011), using galaxy masses from G. Östlin et al. (2001). In the gathered sample at all redshifts, we effectively compare the recently formed mass (within few hundreds of megayears) in clustered (star clusters/clump) systems to the total mass of the galaxy. The high-z galaxies have approximately 2–3 dex higher mass fractions ($\gtrsim$30%) than that measured in local galaxies ($\lesssim$1%). Such high mass fractions are emerging as a preferred trait in lower-mass galaxies at high-z (A. Adamo et al. 2025), as shown by the increasing mass fraction for lower stellar mass (black star symbols in the left panel of Figure 10; A. Claeyssens et al. 2025). Occasionally, due to accretions or merger events, local dwarf galaxies experience an increase in gas pressure and SFR density, resulting in the formation of massive star clusters. However, these events take place in a system where the stellar mass is typically dominated by stellar populations formed over a long timescale. In contrast, for high-z low-mass galaxies, star-forming clumps and star clusters dominate the stellar mass budget of the entire systems. In other words, high-z low-mass

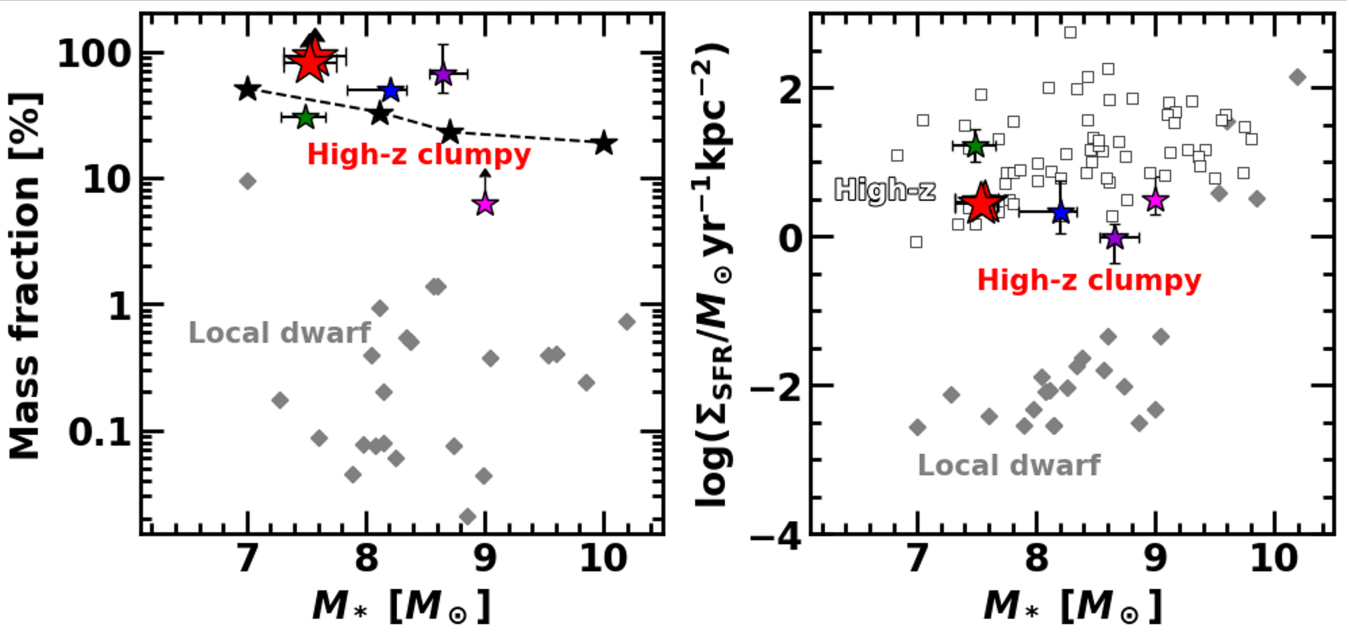


Figure 10. Left: mass fraction in clustered stellar systems as a function of stellar mass. The red star symbols indicate ID1 and ID2 of the Misty Moons ($z_{\rm phot} \sim 11$–12). The blue, green, purple, and magenta star symbols show the BulletArc-z11 ($z_{\rm spec} = 11.10$; M. Bradač et al. 2025), Cosmic Gems arc ($z_{\rm spec} = 9.63$; A. Adamo et al. 2024; L. D. Bradley et al. 2025; M. Messa et al. 2026; E. Vanzella et al. 2026), Cosmic Grapes ($z_{\rm spec} = 6.07$; S. Fujimoto et al. 2025), and Sunburst galaxy ($z_{\rm spec} = 2.37$; E. Vanzella et al. 2022), respectively. The black star symbols denote the median values for clumpy galaxies at $1 < z < 5.5$ (A. Claeyssens et al. 2025). The gray diamonds present the local dwarf galaxies containing young star clusters (A. Adamo et al. 2011; D. Calzetti et al. 2015; D. O. Cook et al. 2023). Right: SFR surface density as a function of stellar mass. The star symbols and diamonds are the same in the left panel. The squares represent spectroscopically confirmed galaxies at $5 < z < 14$ (T. Morishita et al. 2024).

clumpy galaxies might be in a totally different star formation mode, dominated by top down clustered star formation (B. G. Elmegreen 2018).

One of the key differences between the high-z clumpy galaxies and local dwarf galaxies is SFR surface density. As shown in the right panel of Figure 10, the high-z clumpy galaxies exhibit $\sim 10^2$–10^4 times higher SFR surface densities than those of the local dwarf galaxies with similarly low stellar masses of $M_* \sim 10^7$–$10^9 M_\odot$. Considering the positive correlation between cluster formation efficiency and SFR surface density in the local galaxies reported by both observational (e.g., A. Adamo et al. 2020) and theoretical (e.g., J. M. D. Kruijssen 2012; J. Pfeffer et al. 2019) studies, the high SFR density may be a possible driver of the high mass fraction seen in the high-z clumpy galaxies. However, we note that the local BCDs with higher stellar masses of $M_* > 10^9 M_\odot$ have high SFR densities but low-mass fractions compared to the high-z clumpy galaxies. This suggests that high-z clumpy galaxies are likely distinct from the local dwarf galaxies not only in their high SFR surface densities but also in their short, bursty star formation during the early formation phase of the galaxy.

High SFR surface density is associated with high gas density (e.g., R. C. Kennicutt & N. J. Evans 2012), which is a major driver of the violent disk instability, one possible scenario for clump formation at high-z (e.g., A. Dekel et al. 2009, 2013; A. B. Romeo et al. 2010; A. B. Romeo & O. Agertz 2014; S. Fujimoto et al. 2025). Recent simulation results of L. Mayer et al. (2025) have shown that low-mass ($\sim 10^8\, M_\odot$) galaxies form massive self-gravitating compact gas disks, which collapse into massive bound clumps by gravitational instability. We note that although it seems difficult to form stellar disks at this high redshift, some studies suggest possible rotating gas disk formation at $z > 10$ (e.g., Y. Xu et al. 2024; J. Scholtz et al. 2025). The disk instability scenario is consistent with the top-down clump formation suggested by high clustered mass fractions. Regarding the in situ clumps formation, filament fragmentation (e.g., F. A. B. Garcia et al. 2025) and turbulence-driven fragmentation (e.g., M. Dessauges-Zavadsky & A. Adamo 2018) are also suggested as possible scenarios. In recent studies using a cosmological radiation-hydrodynamic simulation (F. A. B. Garcia et al. 2023, 2025), low-mass dwarf galaxies at $z > 8$ with no disk and bulge experience star cluster formation through the fragmentation of accreting dense filaments (i.e., cold inflow) before the gas reached the center. The suppression of cooling via the far-UV (FUV) radiation leads to bursty star formation and massive, compact star clusters (K. Sugimura et al. 2024), sharing the comparable properties with high-z star clusters (L. Mowla et al. 2024; E. Vanzella et al. 2026). These star clusters orbit the center of the dark matter halo, where star formation happens later, resulting in the formation of an NSC (F. A. B. Garcia et al. 2025). Considering that our central clumps (A.1 and A.2) have comparable stellar masses and effective radii to those of NSCs (Figure 7), the filament fragmentation is also a plausible scenario for the clump formation of the Misty Moons.

One of the other possibilities of clump formation is a galaxy merger (e.g., J. Matthee et al. 2017; T. Y.-Y. Hsiao et al. 2023; K. Boyett et al. 2024; C. Marconcini et al. 2024; Y. Nakazato et al. 2024; Y. Harikane et al. 2025; T. Kiyota et al. 2025; A. Bik et al. 2026; R. G. Pascalau et al. 2026). In fact, T. Y.-Y. Hsiao et al. (2023) suggest that the observed clumpy structure of MACS0647-JD at $z_{\rm spec} = 10.17$ could be due to a galaxy merger based on the different SFHs among the clumps

and comparison with some simulation results. In a recent study of M. Kohandel et al. (2025), they identify Amaryllis, a digital twin of $z > 10$ galaxies, in the SERRA zoom-in simulations. At $z > 10$, Amaryllis has a main progenitor and coexisting small companions, which form stars in a clustered and bursty way, and eventually merge. The morphology of Amaryllis is very similar to the Misty Moons (see Figure 1 in M. Kohandel et al. 2025). Observationally, the Misty Moons has stellar ages for the central clumps (A.1 and A.2) that are relatively younger than the other clumps (see Table 3), which might suggest a possible merger scenario. However, the current NIRCam images have almost no coverage of the wavelengths longer than Balmer breaks, which complicates the exact measurements of stellar ages and SFHs enough to conclude that the individual clumps undergo different SFHs. Future observations with NIRSpec/IFU (for gas kinematics and spatial distribution of stellar/gas properties) and MIRI (for metallicity measurement and optical continuum from old stellar populations) are helpful to further explore the clump properties and physical origins of the clump formation.

6. Summary

In this paper, we report the discovery of the Misty Moons, a strongly lensed galaxy at $z \sim 11$–12 behind the galaxy cluster MACS J0257.1-2325, newly identified in the JWST Treasury Survey VENUS. Independent lens models predict that the Misty Moons has five multiple images, two of which, ID1 and ID2 ($\mu \sim 20$–30), are very bright (F200W ~ 26 mag) in the image plane, while intrinsically faint ($M_{\rm UV} \sim -18$) in the source plane, and exhibit blue SEDs with prominent Lyα breaks. In addition, ID1 and ID2 are resolved into multiple clumps in NIRCam images. We summarize our main findings below:

1. We conduct SED fitting to ID1 and ID2 with `EAZY` and `Prospector` to estimate their photometric redshifts and stellar populations. For both the fitting codes, we adopt models excluding and including Lyα emission, resulting in $z_{\rm phot} \sim 11$ and $z_{\rm phot} \sim 12$, respectively. We also fit the individual clumps of ID1 and ID2, fixing the redshift to $z = 11.5$. The SED fitting results show that the entire systems and individual clumps of the Misty Moons consist of young stars ($t \sim 40$–70 Myr with nonparametric SFHs and $t \sim 20$–40 Myr with short SFHs) with low dust content ($A_{\rm V} \lesssim 0.1$ mag), likely undergoing their first significant starbursts.
2. Correcting for the high magnification, ID1 (ID2) is resolved into four (three) clumps with effective radii of $r_{\rm eff} \sim 10$–70 pc and stellar masses of $M_* \sim 10^7\,M_\odot$, which are comparable to those of the local nuclear/young massive star clusters and high-z ($z \gtrsim 6$) star-forming clumps. The Misty Moons exhibit a high clumpiness parameter and clump LF normalized by galaxy stellar mass compared to lower-redshift lensed galaxies and simulated galaxies. In particular, these star-cluster-like clumps have high clustered mass fractions ($\gtrsim$80%), similar to other high-z clumps and star clusters. This suggests that star formation in at least some low-mass galaxies at these early epochs may be strongly clump-dominated, in contrast to compact star clusters observed in local dwarf galaxies, which might be driven by high SFR surface densities and short star formation timescales.
3. We convolve the source-plane image with the JWST/NIRCam point-spread function to produce a mock NIRCam image of the Misty Moons without lensing magnification, and find that the intrinsic galaxy has a radial surface-brightness profile comparable to those of typical faint ($M_{\rm UV} \gtrsim -19$ mag) galaxies at $z \gtrsim 10$, including JADES-GS-z13-0 and JADES-GS-z14-1. This suggests that clump formation may be more common among the low-mass galaxies in the early Universe.

Acknowledgments

We thank anonymous referee for the valuable comments that improved this manuscript. We are grateful to the JADES, RELICS, and VENUS teams for developing their imaging surveys, enabling our research. We thank Mahsa Kohandel and Andrea Pallottini for providing SERRA simulation data and the useful discussion on stellar clumps. We thank Yurina Nakazato for the valuable discussions on clump formation. We thank Bingjie Wang for the helpful discussions on `Prospector` SED fitting. This work is based on observations made with the NASA/ESA/CSA James Webb Space Telescope. The data were obtained from the Mikulski Archive for Space Telescopes (MAST) at the Space Telescope Science Institute (STScI), which is operated by the Association of Universities for Research in Astronomy (AURA), Inc., under NASA contract NAS 5-03127 for JWST. The JWST observations are associated with programs #6882 and #1180 (JADES). This paper is also based on observations made with the NASA/ESA Hubble Space Telescope. The data were obtained from MAST at STScI, which is operated by AURA under NASA contract NAS 5-26555. The HST observations are associated with programs #14096 (RELICS). The authors acknowledge the use of the Canadian Advanced Network For Astronomy Research (CANFAR) Science Platform operated by the Canadian Astronomy Data Center (CADC) and the Digital Research Alliance of Canada (DRAC) with support from the National Research Council for Canada (NRC), the Canadian Space Agency (CSA), CANARIE, and the Canadian Foundation for Innovation(CFI). We acknowledge the support of the Canadian Space Agency (CSA) [25JWGO4A18]. M.N. acknowledges support from KAKENHI grant Nos. 25KJ0828 through Japan Society for the Promotion of Science (JSPS) and from the Japan Foundation for Promotion of Astronomy. S.F. acknowledges support from the Dunlap Institute, funded through an endowment established by the David Dunlap family and the University of Toronto. M.O. acknowledges the support from the World Premier International Research Center Initiative (WPI Initiative), MEXT, Japan, the joint research program of the Institute for Cosmic Ray Research (ICRR), the University of Tokyo, and KAKENHI (20H00180, 21H04467, 25H00674) through JSPS. D.M. acknowledges the support of the Royal Society through the award of a Royal Society University Research Professorship to James S. Dunlop. M.O. acknowledges the support from JSPS KAKENHI grant Numbers JP25H00662, JP22K21349. A.Z. acknowledges support by the Israel Science Foundation grant No. 864/23. A.A. acknowledges support by the Swedish research council Vetenskapsrådet (VR) project 2021-05559, and VR consolidator grant 2024-02061. E.V. and M.M. acknowledge financial

support through grants PRIN-MIUR 2020SKSTHZ, grants INAF GO Grant 2024 "Mapping Star Cluster Feedback in a Galaxy 450 Myr after the Big Bang," and by the European Union—NextGenerationEU within PRIN 2022 project n.20229YBSAN—Globular clusters in cosmological simulations and lensed fields: from their birth to the present epoch. M.B. and G.R. acknowledge support from the ERC Grant FIRSTLIGHT #101053208, Slovenian national research agency ARIS through grants N1-0238 and P1-0188, and ESA PRODEX Experiment Arrangements Nos. 4000146646 and 4000149972. M.M. acknowledges financial support through grants INAF GO Grant 2022 "The revolution is around the corner: JWST will probe globular cluster precursors and Population III stellar clusters at cosmic dawn." H.Y. acknowledges support by KAKENHI (25KJ0832) through JSPS. R.A. acknowledges support of grant PID2023-147386NB-I00 funded by MICIU/AEI/10.13039/501100011033 and by ERDF/EU, and the Severo Ochoa award to the IAA-CSIC CEX2021-001131-S and from grant PID2022- 136598NB-C32 "Estallidos8." H.A. acknowledges support from CNES, focused on the JWST mission, and the French National Research Agency (ANR) under grant ANR-21-CE31-0838. C.J.C. acknowledges support from the ERC Advanced Investigator Grant EPOCHS (788113). P.D. warmly acknowledges support from an NSERC discovery grant (RGPIN-2025-06182). J.M.D. acknowledges the support of projects PID2022-138896NB-C51 (MCIU/AEI/MINECO/FEDER, UE) Ministerio de Ciencia, Investigación. Y.H. acknowledges support from the JSPS Grant-in-Aid for Scientific Research (24H00245) and the JSPS International Leading Research (22K21349). Y.F. acknowledges support from JSPS KAKENHI grant Nos. JP22K21349 and JP23K13149. Y.J.-T. acknowledges financial support from the State Agency for Research of the Spanish MCIU through Center of Excellence Severo Ochoa award to the Instituto de Astrofísica de Andalucía CEX2021-001131-S funded by MCIN/AEI/10.13039/501100011033, and from the grant PID2022-136598NB-C32 Estallidos and project ref. AST22-00001-Subp-15 funded by the EU-NextGenerationEU. T.K acknowledges support by KAKENHI (26KJ1232) through JSPS. G.E.M. acknowledges the Villum Fonden research grants 13160 and 37440 and the Cosmic Dawn Center of Excellence funded by the Danish National Research Foundation under the grant No. 140. G.N. is supported by the Canadian Space Agency under a contract with NRC Herzberg Astronomy and Astrophysics. This work has received funding from the Swiss State Secretariat for Education, Research and Innovation (SERI) under contract No. MB22.00072, as well as from the Swiss National Science Foundation (SNSF) through project grant 200020_207349. The Cosmic Dawn Center (DAWN) is funded by the Danish National Research Foundation under grant DNRF140. R.A.W. acknowledges support from NASA JWST Interdisciplinary Scientist grants NAG5-12460, NNX14AN10G and 80NSSC18K0200 from GSFC. F.E.B. acknowledges support from ANID-Chile BASAL CATA FB210003, FONDECYT Regular 1241005, ECOS-ANID ECOS240037, and Millennium Science Initiative, AIM23-0001. M.G.O acknowledges financial support from the State Agency for Research of the Spanish MCIU through Center of Excellence Severo Ochoa award to the Instituto de Astrofísica de Andalucía CEX2021-001131-S funded by MCIN/AEI/10.13039/501100011033, and from the grant PID2022-136598NB-C32 "Estallidos8" funded by MCIN/AEI/10.13039/501100011033 and by "ERDF A way of making Europe". MGO also acknowledges the support by the project ref. AST22_00001_Subp_11 funded from the EU – NextGenerationEU, PPCC Junta de Andalucía. K.K. acknowledges support from JSPS KAKENHI grant Nos. JP22H04939, JP23K20035, and JP24H00004. I.L. acknowledges support by the Australian Research Council through Future Fellowship FT220100798. R.P.N. is grateful for the generous support of Neil and Jane Pappalardo through the MIT Pappalardo Fellowship. The English in this paper was partially refined with the assistance of ChatGPT (OpenAI).

Software: NumPy (C. R. Harris et al. 2020), matplotlib (J. D. Hunter 2007), SciPy (P. Virtanen et al. 2020), Astropy (Astropy Collaboration et al. 2013, 2018, 2022), `grizli` (G. Brammer 2023a, 2023b), `Photutils` (L. Bradley et al. 2025), `EAZY` (G. B. Brammer et al. 2008), `Prospector` (B. D. Johnson et al. 2021), Glafic (M. Oguri 2010, 2021), `Bagpipes`, (A. C. Carnall et al. 2018), `GALFIT` (C. Y. Peng et al. 2010).

Appendix A
Photometry

In Table A1, we list the photometry of the entire systems and individual clumps for ID1 and ID2 of the Misty Moons. The method is described in Section 2.2.

Table A1
Measured Photomery of the Misty Moons

Name	F435W (nJy)	F555W (nJy)	F814W (nJy)	F090W (nJy)	F115W (nJy)	F150W (nJy)	F200W (nJy)	F210M (nJy)	F277W (nJy)	F300M (nJy)	F356W (nJy)	F410M (nJy)	F444W (nJy)
ID1 (Customized)	-35.3 ± 25.4	5.3 ± 9.1	9.7 ± 7.9	2.9 ± 9.5	-3.7 ± 10.7	80.9 ± 13.7	129.8 ± 13.4	137.4 ± 15.3	118.4 ± 10.5	114.0 ± 12.4	104.7 ± 9.4	77.6 ± 10.5	106.0 ± 10.6
ID1 (Isophoto)	-35.9 ± 33.6	-0.2 ± 11.9	19.1 ± 12.0	8.6 ± 12.3	2.9 ± 13.3	51.6 ± 14.3	133.0 ± 10.6	113.1 ± 14.4	118.4 ± 6.8	106.9 ± 8.2	110.9 ± 6.0	65.6 ± 9.6	125.5 ± 6.8
ID1 (Kron)	-16.6 ± 25.2	12.5 ± 13.7	12.0 ± 8.9	3.5 ± 9.1	-3.3 ± 10.7	82.3 ± 11.4	151.7 ± 9.9	156.7 ± 11.5	130.1 ± 8.7	116.6 ± 9.1	109.5 ± 7.6	74.6 ± 9.8	96.2 ± 8.3
A.1	⋯	⋯	⋯	⋯	⋯	45.7 ± 8.0	63.1 ± 5.2	72.4 ± 5.3	53.5 ± 4.9	55.5 ± 5.6	47.4 ± 4.8	45.7 ± 6.3	47.4 ± 4.8
B.1	⋯	⋯	⋯	⋯	⋯	⋯	20.0 ± 5.0	23.3 ± 5.6	21.3 ± 5.8	24.4 ± 5.9	23.1 ± 6.0	⋯	28.6 ± 5.0
C.1	⋯	⋯	⋯	⋯	⋯	32.5 ± 12.2	48.3 ± 7.6	31.3 ± 6.7	18.2 ± 7.9	15.4 ± 6.9	25.8 ± 8.0	⋯	14.2 ± 6.9
D.1	⋯	⋯	⋯	⋯	⋯	⋯	24.4 ± 7.1	⋯	15.8 ± 5.4	22.9 ± 7.7	14.2 ± 5.3	⋯	17.5 ± 7.1
ID2 (Customized)	-17.3 ± 26.0	-2.8 ± 8.7	11.0 ± 8.5	10.7 ± 10.5	21.8 ± 10.8	69.3 ± 13.0	146.3 ± 14.8	110.8 ± 14.7	110.7 ± 11.6	105.7 ± 11.6	92.0 ± 9.7	95.5 ± 11.9	87.9 ± 10.5
ID2 (Isophoto)	-37.5 ± 32.1	9.0 ± 11.5	26.7 ± 11.2	2.6 ± 11.9	7.4 ± 13.7	51.9 ± 15.0	115.6 ± 10.4	75.5 ± 13.7	110.7 ± 6.3	88.2 ± 8.3	75.3 ± 5.8	86.9 ± 9.3	92.6 ± 6.9
ID2 (Kron)	-23.4 ± 20.0	4.1 ± 11.4	10.4 ± 7.6	7.9 ± 11.2	23.3 ± 13.3	53.4 ± 13.8	137.0 ± 12.4	99.8 ± 13.2	98.4 ± 6.9	87.0 ± 7.8	73.7 ± 7.2	84.9 ± 8.3	64.9 ± 6.9
A.2	⋯	⋯	⋯	⋯	⋯	34.7 ± 4.5	73.8 ± 3.4	54.5 ± 4.0	47.4 ± 3.5	44.5 ± 3.7	42.5 ± 3.5	41.3 ± 3.4	40.2 ± 3.7
B.2	⋯	⋯	⋯	⋯	⋯	⋯	17.2 ± 5.6	⋯	19.2 ± 5.9	18.7 ± 5.8	16.3 ± 6.0	⋯	13.3 ± 5.4
C.2	⋯	⋯	⋯	⋯	⋯	23.1 ± 8.5	26.5 ± 9.2	47.0 ± 8.3	31.9 ± 9.2	17.1 ± 8.1	28.8 ± 9.2	27.0 ± 9.4	30.2 ± 9.3

Note. Observed fluxes, not corrected for magnification. For ID1 and ID2, we present fluxes measured with customized, total isophotal, and Kron apertures (Section 2.2). We use customized aperture (total isophotal) fluxes of ID1 and ID2 to estimate photometric redshift (stellar population). For individual clumps, the fluxes are derived with `GALFIT` fitting.

Appendix B
Surface-brightness Profiles of the Most Compact Clumps

In Section 4.2, we investigate whether the most compact clumps of A.1 and A.2 are spatially resolved by using both Sérsic-profile and pure-PSF fitting to the detection (F200W + F277W + F356W + F444W) and F200W images. To visually examine the light distribution, we measure radial surface-brightness profiles of PSF, clumps A.1, and A.2 by measuring surface brightness in circular annuli centered on the brightest pixels using `Photutils`. The uncertainties are estimated from the corresponding variance images. The resulting surface-brightness profiles are presented in Figure B1. As described in Section 4.2, the clumps are marginally broader than the PSF in the detection image while their profiles in the F200W image are consistent with the PSF within the measurement uncertainties.

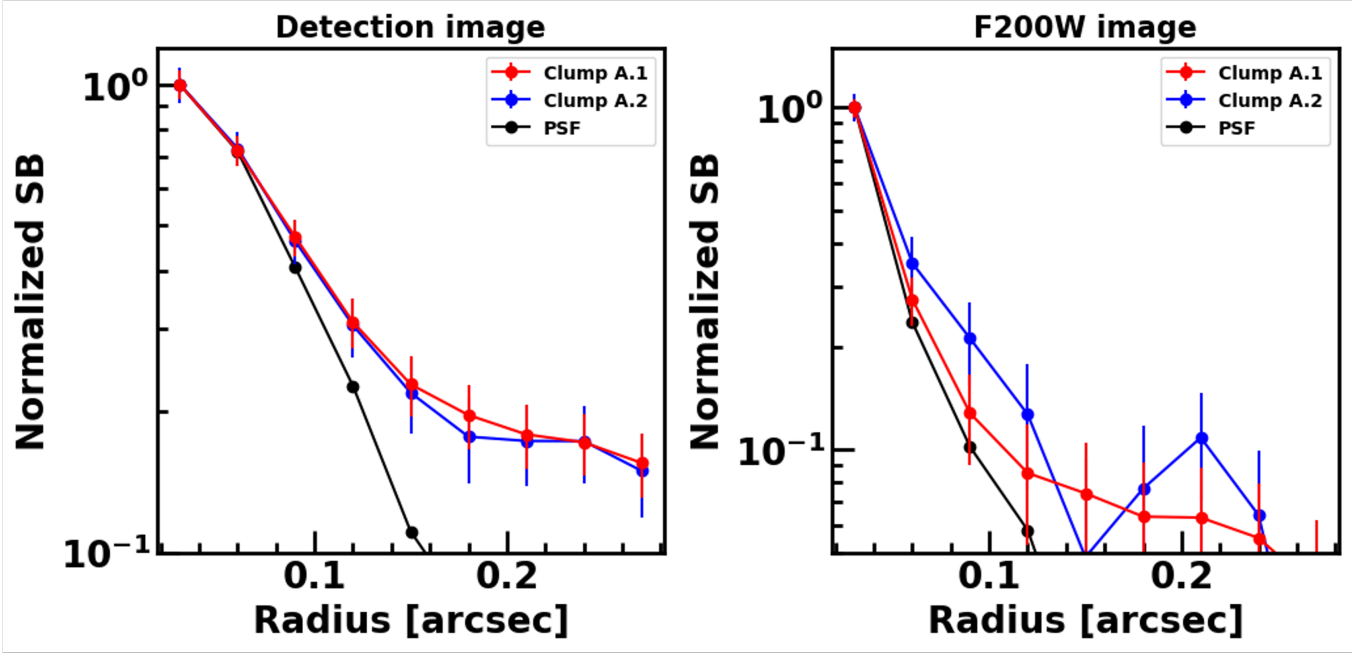


Figure B1. Radial surface-brightness profiles of the most compact clumps A.1 and A.2 in the detection (F200W + F277W + F356W + F444W; left) and F200W images (right). The red, blue, and black circles present the measurements for clumps A.1, A.2, and PSF, respectively.

Appendix C
Effect of Lens Model Uncertainties on Derived Physical Properties

This work is based on two independent lens models described in Section 3. To evaluate the impact of lens model uncertainties on the intrinsic physical properties, we compare the delensed stellar masses and half-light radii derived with the Zitrin-Analytic and Glafic models in Figure C1. The figure shows that the measurements based on the two lens models are consistent within the uncertainties, indicating that the choice of lens model has only a minor impact on our discussion. We note that the surface density estimates are largely insensitive to the lens models because gravitational lensing conserves surface brightness to first order.

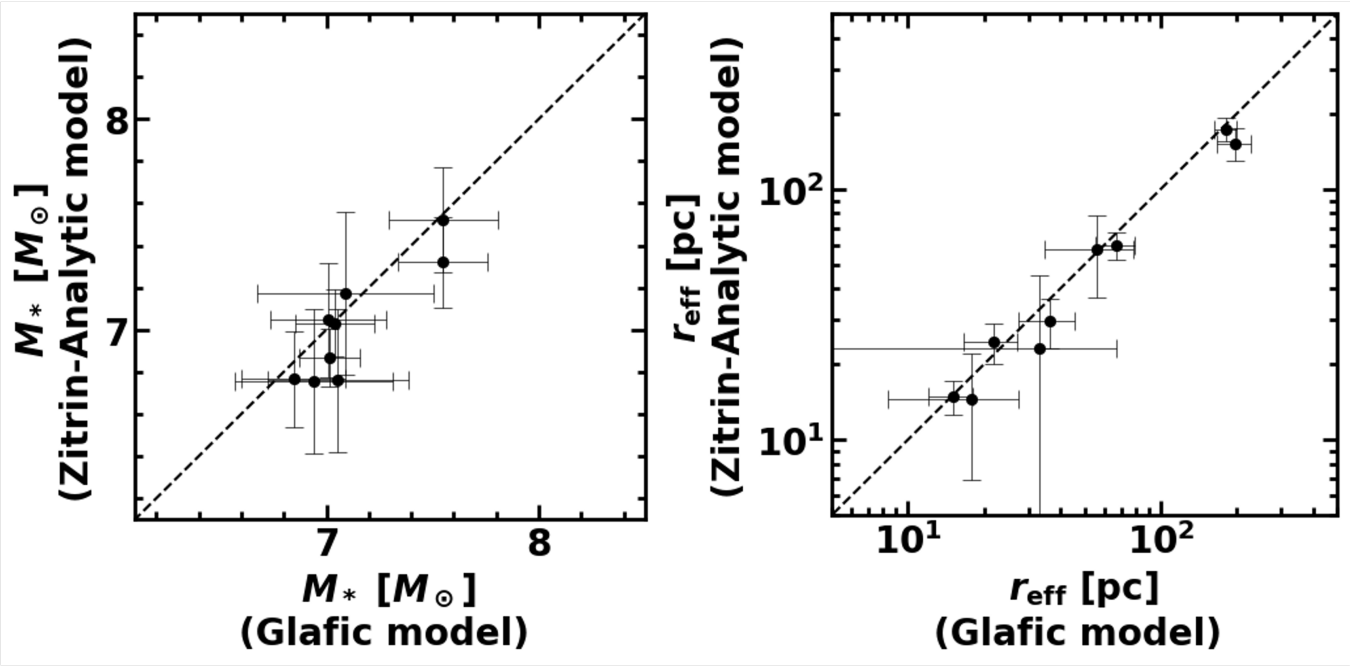


Figure C1. Comparison of intrinsic stellar mass and half-light radius measurements with Zitrin-Analytic and Glafic lens models. The circles present the measurements for the stellar mass (left) and half-light radius (right), and their 1σ uncertainties. The black lines indicate that the physical properties obtained from the two lens models are consistent.

ORCID iDs

Minami Nakane https://orcid.org/0009-0000-1999-5472
Vasily Kokorev https://orcid.org/0000-0002-5588-9156
Seiji Fujimoto https://orcid.org/0000-0001-7201-5066
Masami Ouchi https://orcid.org/0000-0002-1049-6658
Derek J. McLeod https://orcid.org/0000-0003-4368-3326
Miriam Golubchik https://orcid.org/0000-0001-9411-3484
Masamune Oguri https://orcid.org/0000-0003-3484-399X
Adi Zitrin https://orcid.org/0000-0002-0350-4488
Cecilia Bondestam https://orcid.org/0009-0008-3775-5112
Callum T. Donnan https://orcid.org/0000-0002-7622-0208
Gabriel Brammer https://orcid.org/0000-0003-2680-005X
Steven L. Finkelstein https://orcid.org/0000-0001-8519-1130
Chris Willott https://orcid.org/0000-0002-4201-7367
Gregor Rihtaršič https://orcid.org/0009-0009-4388-898X
Guillaume Desprez https://orcid.org/0000-0001-8325-1742
Angela Adamo https://orcid.org/0000-0002-8192-8091
Eros Vanzella https://orcid.org/0000-0002-5057-135X
Maruša Bradač https://orcid.org/0000-0001-5984-0395
Matteo Messa https://orcid.org/0000-0003-1427-2456
Hiroto Yanagisawa https://orcid.org/0009-0006-6763-4245
Fengwu Sun https://orcid.org/0000-0002-4622-6617
Henry C. Ferguson https://orcid.org/0000-0001-7113-2738
Ray A. Lucas https://orcid.org/0000-0003-1581-7825
Dan Coe https://orcid.org/0000-0001-7410-7669
Johan Richard https://orcid.org/0000-0001-5492-1049
Abdurro'uf https://orcid.org/0000-0002-5258-8761
Hollis B. Akins https://orcid.org/0000-0003-3596-8794
Joseph F. V. Allingham https://orcid.org/0000-0003-2718-8640
Ricardo O. Amorín https://orcid.org/0000-0001-5758-1000
Yoshihisa Asada https://orcid.org/0000-0003-3983-5438
Hakim Atek https://orcid.org/0000-0002-7570-0824
Franz E. Bauer https://orcid.org/0000-0002-8686-8737
Rachel Bezanson https://orcid.org/0000-0001-5063-8254
Larry D. Bradley https://orcid.org/0000-0002-7908-9284
John Chisholm https://orcid.org/0000-0002-0302-2577
Christopher J. Conselice https://orcid.org/0000-0003-1949-7638
Pratika Dayal https://orcid.org/0000-0001-8460-1564
Miroslava Dessauges-Zavadsky https://orcid.org/0000-0003-0348-2917
Jose M. Diego https://orcid.org/0000-0001-9065-3926
Andreas L. Faisst https://orcid.org/0000-0002-9382-9832
Gavin Farley https://orcid.org/0009-0007-2578-9238
Qinyue Fei https://orcid.org/0000-0001-7232-5355
Brenda L. Frye https://orcid.org/0000-0003-1625-8009
Yoshinobu Fudamoto https://orcid.org/0000-0001-7440-8832
Lukas J. Furtak https://orcid.org/0000-0001-6278-032X
Yuichi Harikane https://orcid.org/0000-0002-6047-430X
Tiger Yu-Yang Hsiao https://orcid.org/0000-0003-4512-8705
Yolanda Jiménez-Teja https://orcid.org/0000-0002-6090-2853
Jeyhan S. Kartaltepe https://orcid.org/0000-0001-9187-3605
Tomokazu Kiyota https://orcid.org/0009-0004-4332-9225
Anton M. Koekemoer https://orcid.org/0000-0002-6610-2048
Claudia del P. Lagos https://orcid.org/0000-0003-3021-8564
Georgios E. Magdis https://orcid.org/0000-0002-4872-2294
Ashish Kumar Meena https://orcid.org/0000-0002-7876-4321
Lamiya Mowla https://orcid.org/0000-0002-8530-9765
Pascal A. Oesch https://orcid.org/0000-0001-5851-6649
Yoshiaki Ono https://orcid.org/0000-0001-9011-7605
Rafael Ortiz, III https://orcid.org/0000-0002-6150-833X
Richard Pan https://orcid.org/0000-0002-9651-5716
Casey Papovich https://orcid.org/0000-0001-7503-8482
Justin D. R. Pierel https://orcid.org/0000-0002-2361-7201
Massimo Ricotti https://orcid.org/0000-0003-4223-7324
Luke Robbins https://orcid.org/0000-0002-6265-2675
Daniel Schaerer https://orcid.org/0000-0001-7144-7182
Raffaella Schneider https://orcid.org/0000-0001-9317-2888
Tommaso Treu https://orcid.org/0000-0002-8460-0390
Francesco Valentino https://orcid.org/0000-0001-6477-4011
Rogier A. Windhorst https://orcid.org/0000-0001-8156-6281
Volker Bromm https://orcid.org/0000-0003-0212-2979
Eiichi Egami https://orcid.org/0000-0003-1344-9475
Mauro González-Otero https://orcid.org/0000-0002-4837-1615
Kotaro Kohno https://orcid.org/0000-0002-4052-2394
Ivo Labbe https://orcid.org/0000-0002-2057-5376
Jorryt Matthee https://orcid.org/0000-0003-2871-127X
Marcie Mun https://orcid.org/0000-0002-3706-9955
Rohan P. Naidu https://orcid.org/0000-0003-3997-5705
Roberta Tripodi https://orcid.org/0000-0002-9909-3491

References

Abdurro'uf, Coe, D., Resseguier, T., et al. 2025, arXiv:2512.08054
Adamo, A., Atek, H., Bagley, M. B., et al. 2025, NatAs, 9, 1134
Adamo, A., Bradley, L. D., Vanzella, E., et al. 2024, Natur, 632, 513
Adamo, A., Östlin, G., & Zackrisson, E. 2011, MNRAS, 417, 1904
Adamo, A., Zeidler, P., Kruijssen, J. M. D., et al. 2020, SSRv, 216, 69
Arrabal Haro, P., Dickinson, M., Finkelstein, S. L., et al. 2023, ApJL, 951, L22
Asada, Y., Desprez, G., Willott, C. J., et al. 2025, ApJL, 983, L2
Astropy Collaboration, Price-Whelan, A. M., Lim, P. L., et al. 2022, ApJ, 935, 167
Astropy Collaboration, Price-Whelan, A. M., Sipőcz, B. M., et al. 2018, AJ, 156, 123
Astropy Collaboration, Robitaille, T. P., Tollerud, E. J., et al. 2013, A&A, 558, A33
Behroozi, P., Wechsler, R. H., Hearin, A. P., & Conroy, C. 2019, MNRAS, 488, 3143
Berkheimer, J. M., Windhorst, R. A., Harris, W. E., et al. 2026, AJ, 171, 48
Bik, A., Álvarez-Márquez, J., Crespo Gómez, A., et al. 2026, arXiv:2604.22460
Boyett, K., Trenti, M., Leethochawalit, N., et al. 2024, NatAs, 8, 657
Bradač, M., Judež, J., Willott, C., et al. 2025, ApJ, 995, 74
Bradač, M., Strait, V., Mowla, L., et al. 2024, ApJL, 961, L21
Bradley, L., Sipőcz, B., Robitaille, T., et al. 2025, astropy/photutils: v2.2.0, doi:10.5281/zenodo.14889440
Bradley, L. D., Adamo, A., Vanzella, E., et al. 2025, ApJ, 991, 32
Bradley, L. D., Coe, D., Brammer, G., et al. 2023, ApJ, 955, 13
Brammer, G. 2023a, grizli, v1.9.11, doi:10.5281/zenodo.1146904
Brammer, G. 2023b, grizli, v1.9.11, doi:10.5281/zenodo.8370018
Brammer, G. B., van Dokkum, P. G., & Coppi, P. 2008, ApJ, 686, 1503
Brown, G., & Gnedin, O. Y. 2021, MNRAS, 508, 5935
Bruzual, G., & Charlot, S. 2003, MNRAS, 344, 1000
Bunker, A. J., Saxena, A., Cameron, A. J., et al. 2023, A&A, 677, A88
Calabrò, A., Daddi, E., Fensch, J., et al. 2019, A&A, 632, A98
Calzetti, D., Armus, L., Bohlin, R. C., et al. 2000, ApJ, 533, 682

Calzetti, D., Lee, J. C., Sabbi, E., et al. 2015, AJ, 149, 51
Carnall, A. C., McLure, R. J., Dunlop, J. S., & Davé, R. 2018, MNRAS, 480, 4379
Carniani, S., Hainline, K., D'Eugenio, F., et al. 2024, Natur, 633, 318
Castellano, M., Napolitano, L., Fontana, A., et al. 2024, ApJ, 972, 143
Chabrier, G. 2003, PASP, 115, 763
Charlot, S., & Fall, S. M. 2000, ApJ, 539, 718
Choi, J., Dotter, A., Conroy, C., et al. 2016, ApJ, 823, 102
Claeyssens, A., Adamo, A., Messa, M., et al. 2025, MNRAS, 537, 2535
Coe, D., Salmon, B., Bradač, M., et al. 2019, ApJ, 884, 85
Conroy, C., & Gunn, J. E. 2010, ApJ, 712, 833
Conselice, C. J., Bershady, M. A., Dickinson, M., & Papovich, C. 2003, AJ, 126, 1183
Cook, D. O., Lee, J. C., Adamo, A., et al. 2023, MNRAS, 519, 3749
Curtis-Lake, E., Carniani, S., Cameron, A., et al. 2023, NatAs, 7, 622
Dekel, A., Sari, R., & Ceverino, D. 2009, ApJ, 703, 785
Dekel, A., Zolotov, A., Tweed, D., et al. 2013, MNRAS, 435, 999
Dessauges-Zavadsky, M., & Adamo, A. 2018, MNRAS, 479, L118
D'Eugenio, F., Maiolino, R., Carniani, S., et al. 2024, A&A, 689, A152
Eldridge, J. J., Stanway, E. R., Xiao, L., et al. 2017, PASA, 34, e058
Elíasdóttir, Á., Limousin, M., Richard, J, et al. 2007, arXiv:0710.5636
Elmegreen, B. G. 2018, ApJ, 869, 119
Endsley, R., Stark, D. P., Whitler, L., et al. 2024, MNRAS, 533, 1111
Ferland, G. J., Chatzikos, M., Guzmán, F., et al. 2017, RMxAA, 53, 385
Fujimoto, S., Ouchi, M., Kohno, K., et al. 2025, NatAs, 9, 1553
Fujimoto, S., Wang, B., Weaver, J. R., et al. 2024, ApJ, 977, 250
Furtak, L. J., Zitrin, A., Richard, J., et al. 2024, MNRAS, 533, 2242
Furtak, L. J., Zitrin, A., Weaver, J. R., et al. 2023, MNRAS, 523, 4568
Garcia, F. A. B., Ricottai, M., Sugimura, K., & Park, J. 2023, MNRAS, 522, 2495
Garcia, F. A. B., Ricotti, M., & Sugimura, K. 2025, OJAp, 8, 146
Gehrels, N. 1986, ApJ, 303, 336
Goddard, Q. E., Bastian, N., & Kennicutt, R. C. 2010, MNRAS, 405, 857
Hainline, K. N., D'Eugenio, F., Jakobsen, P., et al. 2024, ApJ, 976, 160
Harikane, Y., Inoue, A. K., Ellis, R. S., et al. 2025, ApJ, 980, 138
Harikane, Y., Nakajima, K., Ouchi, M., et al. 2024, ApJ, 960, 56
Harikane, Y., Ouchi, M., Oguri, M., et al. 2023, ApJS, 265, 5
Harris, C. R., Millman, K. J., van der Walt, S. J., et al. 2020, Natur, 585, 357
Harris, W. E., Reina-Campos, M., Koekemoer, A. M., et al. 2025, ApJ, 991, 7
Hsiao, T. Y.-Y., Abdurro'uf, Coe, D., et al. 2024, ApJ, 973, 8
Hsiao, T. Y.-Y., Coe, D., Abdurro'uf, et al. 2023, ApJL, 949, L34
Hunter, J. D. 2007, CSE, 9, 90
Inoue, A. K., Shimizu, I., Iwata, I., & Tanaka, M. 2014, MNRAS, 442, 1805
Isobe, Y., Maiolino, R., D'Eugenio, F., et al. 2025, MNRAS, 541, L71
Isobe, Y., Ouchi, M., Nakajima, K., et al. 2023a, ApJ, 956, 139
Isobe, Y., Ouchi, M., Tominaga, N., et al. 2023b, ApJ, 959, 100
Ji, X., Belokurov, V., Maiolino, R., et al. 2026, MNRAS, 545, staf2110
Johnson, B. D., Leja, J., Conroy, C., & Speagle, J. S. 2021, ApJS, 254, 22
Kalita, B. S., Silverman, J. D., Daddi, E., et al. 2024, ApJ, 960, 25
Keeton, C. R. 2001, arXiv:astro-ph/0102341
Kennicutt, R. C., & Evans, N. J. 2012, ARA&A, 50, 531
Kiyota, T., Ouchi, M., Xu, Y., et al. 2025, ApJ, 995, 150
Kohandel, M., Pallottini, A., & Ferrara, A. 2025, A&A, 704, A39
Kokorev, V., Atek, H., Chisholm, J., et al. 2025a, ApJL, 983, L22
Kokorev, V., Brammer, G., Fujimoto, S., et al. 2022, ApJS, 263, 38
Kokorev, V., Chávez Ortiz, Ó. A., Taylor, A. J., et al. 2025b, ApJL, 988, L10
Kron, R. G. 1980, ApJS, 43, 305
Kruijssen, J. M. D. 2012, MNRAS, 426, 3008
Lagattuta, D. J., Richard, J., Ebeling, H., et al. 2023, MNRAS, 522, 1091
Larson, R. L., Hutchison, T. A., Bagley, M., et al. 2023, ApJ, 958, 141
Limousin, M., Richard, J., Kneib, J.-P., et al. 2008, A&A, 489, 23
Livermore, R. C., Jones, T. A., Richard, J., et al. 2015, MNRAS, 450, 1812
Madau, P. 1995, ApJ, 441, 18
Maiolino, R., Scholtz, J., Witstok, J., et al. 2024, Natur, 627, 59
Marconcini, C., D'Eugenio, F., Maiolino, R., et al. 2024, MNRAS, 533, 2488
Matthee, J., Sobral, D., Boone, F., et al. 2017, ApJ, 851, 145
Mayer, L., van Donkelaar, F., Messa, M., Capelo, P. R., & Adamo, A. 2025, ApJL, 981, L28
McLeod, D. J., Donnan, C. T., McLure, R. J., et al. 2024, MNRAS, 527, 5004
Meena, A. K., & Bagla, J. S. 2020, MNRAS, 492, 3294
Messa, M., Adamo, A., Östlin, G., et al. 2018, MNRAS, 473, 996
Messa, M., Vanzella, E., Loiacono, F., et al. 2025, A&A, 694, A59
Messa, M., Vanzella, E., Loiacono, F., et al. 2026, A&A, 705, A173
Morishita, T., Stiavelli, M., Chary, R.-R., et al. 2024, ApJ, 963, 9
Mowla, L., Iyer, K., Asada, Y., et al. 2024, Natur, 636, 332
Naidu, R. P., Oesch, P. A., Brammer, G., et al. 2026, OJAp, 9
Nakazato, Y., Ceverino, D., & Yoshida, N. 2024, ApJ, 975, 238
Napolitano, L., Castellano, M., Pentericci, L., et al. 2025, A&A, 693, A50
Narayanan, D., Lower, S., Torrey, P., et al. 2024, ApJ, 961, 73
Navarro, J. F., Frenk, C. S., & White, S. D. M. 1996, ApJ, 462, 563
Norris, M. A., Kannappan, S. J., Forbes, D. A., et al. 2014, MNRAS, 443, 1151
Oguri, M. 2010, PASJ, 62, 1017
Oguri, M. 2021, PASP, 133, 074504
Oke, J. B., & Gunn, J. E. 1983, ApJ, 266, 713
Ono, Y., Ouchi, M., Harikane, Y., et al. 2025, ApJ, 991, 222
Östlin, G., Amram, P., Bergvall, N., et al. 2001, A&A, 374, 800
Pallottini, A., Ferrara, A., Gallerani, S., et al. 2022, MNRAS, 513, 5621
Pascalau, R. G., D'Eugenio, F., Maiolino, R., et al. 2026, MNRAS, 551, 1369
Pascale, M., Frye, B. L., Diego, J., et al. 2022, ApJL, 938, L6
Peng, C. Y., Ho, L. C., Impey, C. D., & Rix, H.-W. 2010, AJ, 139, 2097
Pfeffer, J., Bastian, N., Kruijssen, J. M. D., et al. 2019, MNRAS, 490, 1714
Pillepich, A., Nelson, D., Springel, V., et al. 2019, MNRAS, 490, 3196
Rigby, J., Perrin, M., McElwain, M., et al. 2023, PASP, 135, 048001
Roberts-Borsani, G., Treu, T., Shapley, A., et al. 2024, ApJ, 976, 193
Romeo, A. B., & Agertz, O. 2014, MNRAS, 442, 1230
Romeo, A. B., Burkert, A., & Agertz, O. 2010, MNRAS, 407, 1223
Sánchez-Blázquez, P., Peletier, R. F., Jiménez-Vicente, J., et al. 2006, MNRAS, 371, 703
Schaerer, D., Marques-Chaves, R., Xiao, M., & Korber, D. 2024, A&A, 687, L11
Scholtz, J., Parlanti, E., Carniani, S., et al. 2025, MNRAS, 544, 113
Schouws, S., Bouwens, R. J., Ormerod, K., et al. 2025, ApJ, 988, 19
Senchyna, P., Plat, A., Stark, D. P., et al. 2024, ApJ, 966, 92
Stanway, E. R., & Eldridge, J. J. 2018, MNRAS, 479, 75
Stiavelli, M., Morishita, T., Chiaberge, M., et al. 2023, ApJL, 957, L18
Sugimura, K., Ricotti, M., Park, J., Garcia, F. A. B., & Yajima, H. 2024, ApJ, 970, 14
Tang, M., Stark, D. P., Mason, C. A., et al. 2026, ApJ, 1001, 38
Topping, M. W., Stark, D. P., Senchyna, P., et al. 2024, MNRAS, 529, 3301
Topping, M. W., Stark, D. P., Senchyna, P., et al. 2025, ApJ, 980, 225
Vanzella, E., Castellano, M., Bergamini, P., et al. 2022, A&A, 659, A2
Vanzella, E., Claeyssens, A., Welch, B., et al. 2023, ApJ, 945, 53
Vanzella, E., Messa, M., Adamo, A., et al. 2026, A&A, 705, A171
Virtanen, P., Gommers, R., Oliphant, T. E., et al. 2020, NaMe, 17, 261
Wang, B., Leja, J., Bezanson, R., et al. 2023, ApJL, 944, L58
Wang, B., Leja, J., Labbé, I., et al. 2024, ApJS, 270, 12
Weaver, J. R., Cutler, S. E., Pan, R., et al. 2024, ApJS, 270, 7
Webb, J. J., & Leigh, N. W. C. 2015, MNRAS, 453, 3278
Wetzel, A., Hayward, C. C., Sanderson, R. E., et al. 2023, ApJS, 265, 44
Whitaker, K. E., Labbé, I., van Dokkum, P. G., et al. 2011, ApJ, 735, 86
Williams, H., Kelly, P. L., Chen, W., et al. 2023, Sci, 380, 416
Witstok, J., Jakobsen, P., Maiolino, R., et al. 2025, Natur, 639, 897
Xu, Y., Ouchi, M., Yajima, H., et al. 2024, ApJ, 976, 142
Yanagisawa, H., Ouchi, M., Nakajima, K., et al. 2025, ApJ, 988, 86
Zanella, A., Pallottini, A., Ferrara, A., et al. 2021, MNRAS, 500, 118
Zavala, J. A., Bakx, T., Mitsuhashi, I., et al. 2024, ApJL, 977, L9
Zitrin, A., Broadhurst, T., Barkana, R., Rephaeli, Y., & Benítez, N. 2011, MNRAS, 410, 1939
Zitrin, A., Fabris, A., Merten, J., et al. 2015, ApJ, 801, 44